공학석사 학위논문

UAV LiDAR Monitoring of Consolidation Settlement during Construction on Reclaimed Land

− A Case Study in Busan, South Korea −

대한민국 부산의 준설매립 시공 현장에 대한 드론라이다 기반 압밀침하 모니터링

2023 년 8 월

서울대학교 대학원

건설환경 공학부

고 석 준

UAV LiDAR Monitoring of Consolidation Settlement during Construction on Reclaimed Land

– A Case Study in Busan, South Korea –

대한민국 부산의 준설매립 시공 현장에 대한 드론라이다 기반 압밀침하 모니터링

지도 교수 김 성 렬

이 논문을 공학석사 학위논문으로 제출함
2023년 8 월

서울대학교 대학원
건설환경공학부
고 석 준

고석준의 석사 학위논문을 인준함
2023년 8 월

위 원 장 _____ 정 충 기 _____ (인)

부위원장 _____ 김 성 렬 _____ (인)

위 원 _____ 박 준 범 _____ (인)

Abstract

UAV LiDAR Monitoring of Consolidation Settlement during Construction on Reclaimed Land

Ko, Seok Jun
Department of Civil and Environmental Engineering
The Graduate School
Seoul National University

In Korea, when monitoring the consolidation settlement of cohesive soil on construction site, measurements are only taken at a relatively small number of points compared to the large area of the site. Due to the uncertainty of soil profile and ground improvement conditions, excessive settlement may occur at locations where settlement is not measured. Recent advances in remote sensing technology have enabled the development of innovative researches for measuring ground deformation. In this study, a method for monitoring the consolidation settlement of the entire construction site in Busan Newport was proposed using Unmanned Aerial Vehicle (UAV) Light Detection and Ranging (LiDAR) measurements. First, the data processing of 3D point cloud was implemented. Among the three conditions and three methods considered, the SOR method was identified as the optimal method for denoising UAV LiDAR data. The optimal grid size was determined to be 50cm×50cm by comparing the results with GPS and TS measurements. Second, the

distribution of consolidation settlement was investigated. Based on the monthly settlement rate at the reference section, a deviation of 0.25m/month was detected, indicating the occurrence of potential differential settlement. The analysis of cumulative settlement for different section sizes indicated that smaller sections captured localized settlement behavior while larger sections exhibited significant variances. Thus, it was concluded that the practical spacing of 100m×100m is not suitable for representing the entire construction site. Third, settlement prediction using the hyperbolic method was conducted. To ensure accurate predictions, the optimal section size was determined by comparing the predicted final settlement based on different section sizes. The section size of 10m×10m was identified as the optimal choice, showing the error of 4cm. Additionally, the required number of measurement points was investigated, increasing the number of points from four to seven. The optimal number of measurement points was determined to be seven, as it resulted in a prediction error below 1%. Through the proposed analysis, the degree of consolidation across the entire site was explored. These findings provide valuable insights for settlement monitoring during preloading on reclaimed land.

Keywords: Drone, LiDAR data processing, Consolidation settlement, Reclamation, Settlement prediction

Student Number: 2021-28403

Contents

Chapter 1 Introduction 1

1.1 Background 1

1.2 Objective 3

1.3 Outline 3

Chapter 2 Literature Review 5

2.1 Introduction 5

2.2 UAV Monitoring for Ground Deformation 5

2.2.1 UAV Photogrammetry 5

2.2.2 UAV and Laser Scanning 7

2.3 3D Point Cloud Data Processing 9

2.3.1 Denoising of Point Cloud Data 9

2.3.2 Bare-earth Filtering 10

2.3.3 Interpolation 11

2.4 Analysis of Consolidation Settlement 11

2.4.1 Mapping of Settlement Rate 11

2.4.2 Settlement Prediction 13

2.5 Summary 15

Chapter 3 Study Site and Measurements 16

3.1 Study Site 16

3.1.1 Overview of Busan Newport 16

3.1.2 Geotechnical Properties 18

3.2 Measurements 20

3.2.1 UAV LiDAR 20
3.2.2 Settlement Plate 22
3.3 Summary 22

Chapter 4 Data Processing of 3D Point Cloud.....23
4.1 Pre-processing 23
4.1.1 Methodology.....23
4.1.2 Correction of Geoid Height 24
4.1.3 Comparison of Denoising Methods.....25
4.2 Interpolation 28
4.2.1 Methodology.....28
4.2.2 Interpolation on Bare-earth.....28
4.2.3 Interpolation on Settlement Plate 30
4.3 Filtering 34
4.3.1 Methodology.....34
4.3.2 Bare-earth Filtering.....35
4.4 Summary 38

Chapter 5 Visualization of Consolidation Settlement 39
5.1 Methodology 39
5.2 Monthly Settlement Rate 40
5.3 Consolidation Settlement Distribution.....45
5.4 Summary 50

Chapter 6 Analysis of Settlement Prediction 51
6.1 Methodology 51

6.2 Settlement Prediction by Hyperbolic Method.....52
6.3 Consolidation Settlement Monitoring.....60
6.4 Summary.....63

Chapter 7 Conclusions 64

References 66

Abstract 71

List of Tables

Table 4.1 Normal vector and distance error according to denoising methods on various conditions 27
Table 4.2 Measurement error on bare-earth according to grid size 30
Table 4.3 Point density on reference plate 32
Table 4.4 Measurement error on settlement plate according to grid size 33
Table 6.1 Prediction accuracy of final settlement according to section size 57
Table 6.2 Prediction accuracy of final settlement according to number of measurements 59

List of Figures

Figure 2.1 Digital elevation model of the tailing surface from UAV-SfM (Rauhala et al., 2017) 6
Figure 2.2 Visualization of cut-fill volume calculation from UAV-SfM (Siebert and Teizer, 2014) 6
Figure 2.3 Profile curve of elevation model from UAV-SfM and TLS (Inzerillo et al., 2018) 7
Figure 2.4 Digital surface model from UAV LiDAR (Lee and Park, 2019) 8
Figure 2.5 Visualization of denoising from UAV LiDAR (Choi et al., 2022)... 9
Figure 2.6 Schematic of the cloth simulation algorithm (Zhang et al., 2016). 10
Figure 2.7 Visualization of annual settlement rate from UAV-SfM (Rauhala et al., 2017) 12
Figure 2.8 Visualization of annual vertical and horizontal displacement from InSAR (Hue et al., 2017) 13
Figure 2.9 The predicted settlement based on hyperbolic and three-point modified exponential method from InSAR (Yu et al., 2021)..... 14
Figure 3.1 Location of the study site 17
Figure 3.2 Geotechnical properties of the study site 19
Figure 3.3 Instrumentations used in this study 21
Figure 4.1 Flowchart of settlement monitoring through UAV LiDAR 24
Figure 4.2 Point cloud results according to denoising method on various conditions: (a-c) raw data; (d-f) denoised data; 25
Figure 4.3 Normal vector and distance error according to denoising methods on various conditions 26
Figure 4.4 Measurement error on bare-earth acording to grid size 29
Figure 4.5 Point cloud results on settlement plate 31
Figure 4.6 Measurement error on settlement plate according to grid size 33
Figure 4.7 Comparison of settlement between UAV LiDAR and total station 34

Figure 4.8 Comparison of CSF results on construction materials 37
Figure 5.1 Procedure of time-series settlement data correction during staged loading 40
Figure 5.2 Visualization of monthly changes in ground elevation 42
Figure 5.3 Monthly settlement rate at the reference section 43
Figure 5.4 Distribution of monthly settlement rate at the reference section ... 45
Figure 5.5 Cumulative settlement-time curve with range of settlement according to section size 46
Figure 6.1 Distribution of cumulative settlement according to section size ... 53
Figure 6.2 Settlement prediction results based on hyperbolic method according to section size 54
Figure 6.3 Settlement prediction results based on number of measurements . 58
Figure 6.4 Cumulative settlement during UAV LiDAR monitoring 61
Figure 6.5 Final settlement predicted by hyperbolic method during UAV LiDAR monitoring..... 61
Figure 6.6 Degree of consolidation according to hyperbolic method during UAV LiDAR monitoring..... 62

Chapter 1 Introduction

1.1 Background

The reclaimed construction site with soft cohesive soil is susceptible to settlement, emphasizing the importance of settlement measurement (Feng et al., 2020; Martín-Antón et al., 2016; Ramirez & Kwon, 2022). If settlement is not properly measured, it can lead to continuous post-construction settlement and induce differential settlement-related cracking in structures (Fei et al., 2013). Settlement occurs in three forms: immediate settlement, primary consolidation settlement, and secondary compression settlement. Most settlement occurs during the primary consolidation process, which can last from several months to several years during the construction period (Shi et al., 2019). In reclaimed construction site, where pore water dissipation takes a long time, it is crucial to implement ground improvement techniques to facilitate the early manifestation of settlement.

In construction sites, settlement measurement for ground improvement is performed using settlement plates. However, measurement is only performed at a relatively small amount of points in comparison to the large area of the site, resulting in insufficient verification of the effectiveness of ground improvement (Shi et al., 2019). Even adjacent areas of soil can have significantly different subsurface conditions, which increases the risk of differential settlement in areas without instrumentation (Muhammed et al., 2020). To precisely simulate the settlement behavior on site, a remote sensing

technology that can measure a wide range of construction sites in a short time and obtain high resolution data is required.

Recently, researches have been actively conducted to acquire three-dimensional ground deformation data using advanced measurement tools such as Unmanned Aerial Vehicle (UAV). Lee & Park (2019) compared the accuracy of UAV LiDAR-based settlement measurements with UAV photogrammetry in urban areas. According to this study, it was recommended to use UAV LiDAR for large areas such as construction sites, due to its ability to monitor with high accuracy. However, researches on settlement through UAV LiDAR measurements at construction sites are still limited.

Therefore, this paper aims to propose a method to monitor consolidation settlement using UAV LiDAR measurements in the preloading area of the Busan Newport construction site, which was constructed by land reclamation. Three main steps were conducted to construct the Digital Elevation Model (DEM) of consolidation settlement: selecting an appropriate denoising technique; determining the optimal grid for DEM construction; selecting suitable bare-earth filtering parameters. Through the constructed DEM, the distribution of consolidation settlement was investigated. Additionally, hyperbolic based settlement prediction was conducted based on the optimal section size and the number of measurements. Consequently, the degree of consolidation across the entire site was explored. This study can be utilized for comprehensive settlement monitoring of the entire construction site on reclaimed land.

1.2 Objective

The purpose of this study is to monitor the consolidation settlement behavior of reclaimed construction site through UAV LiDAR. In summary, the main objectives are as follows:

(a) Determine the suitable 3D point cloud processing method for the construction site: denoising; interpolation; bare-earth filtering;

(b) Suggest an optimal section size and the number of measurements for settlement prediction through UAV LiDAR monitoring

(c) Monitor the degree of consolidation across the entire construction site through UAV LiDAR monitoring

1.3 Outline

This paper documents the monitoring of consolidation settlement of construction site on reclaimed land through UAV LiDAR. The thesis consists of seven chapters which are introduced as follows:

In Chapter 1, background, objective, and outline were presented.

In Chapter 2, a literature review was conducted to outline the researches of UAV monitoring for ground deformation, as well as the analysis of consolidation settlement that have been adopted by past studies. Through the literature review, the limitations of existing research on consolidation settlement monitoring through UAV LiDAR were identified.

In Chapter 3, study site and measurements were explained. Overview and geotechnical properties of the study site were presented. The specification of measurements including UAV LiDAR and settlement plate was explained.

In Chapter 4, data processing of 3d point cloud was provided. Pre-processing was performed including correction of geoid height and denoising method. Interpolation was conducted both on bare-earth and settlement plate. Additionally, bare-earth filtering was utilized and optimal parameters were determined.

In Chapter 5, distribution of consolidation settlement was visualized. Monthly settlement rate at the reference section was investigated. Moreover, the distribution of cumulative settlement was examined according to different section sizes.

In Chapter 6, analysis of settlement prediction was presented. To ensure accurate settlement predictions, the optimal section size and the number of measurements were determined. Through the proposed analysis, the degree of consolidation settlement was explored and visualized.

In Chapter 7, a summary of conclusions was provided.

Chapter 2 Literature Review

2.1 Introduction

Recently, the use of UAV to obtain three-dimensional ground deformation data has been actively explored in remote sensing. Various studies have been conducted to analyze the ground deformation characteristics based on UAV, such as in mines (Rauhala et al., 2017), urban areas (Lee & Park, 2019), and fault (Yang et al., 2022). There are two main methods for constructing 3D point clouds from 2D imagery.

2.2 UAV Monitoring for Ground Deformation

2.2.1 UAV Photogrammetry

The first is UAV-Structure from Motion (SfM), which obtains 3D point clouds by acquiring UAV-based 2D imagery from multiple angles. In 2017, UAV-SfM was used to analyze the settlement of mine tailing impoundment (Rauhala et al., 2017). The DEM constructed from this (Fig. 2.1) was used to visualize or analyze the long-term settlement rate based on the DEMS of Differences (DoDs). However, it was reported that the accuracy of UAV-SfM decreases when the area is wide, making it difficult to use. UAV-SfM based DoDs have also been used to produce cut-fill analysis (Fig. 2.2) to calculate the volume of soil for use in civil engineering of the construction site (Kim et al., 2021; Lee & Lee, 2022; Siebert & Teizer, 2014).

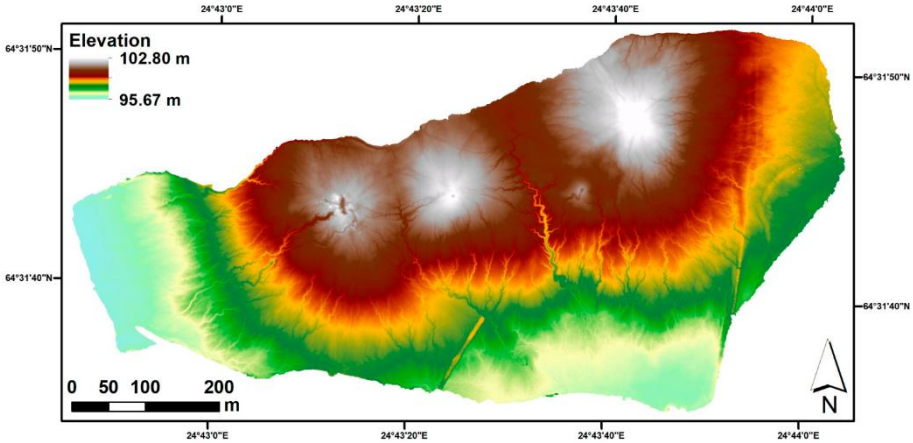

Figure 2.1 Digital elevation model of the tailing surface from UAV-SfM

(Rauhala et al., 2017)

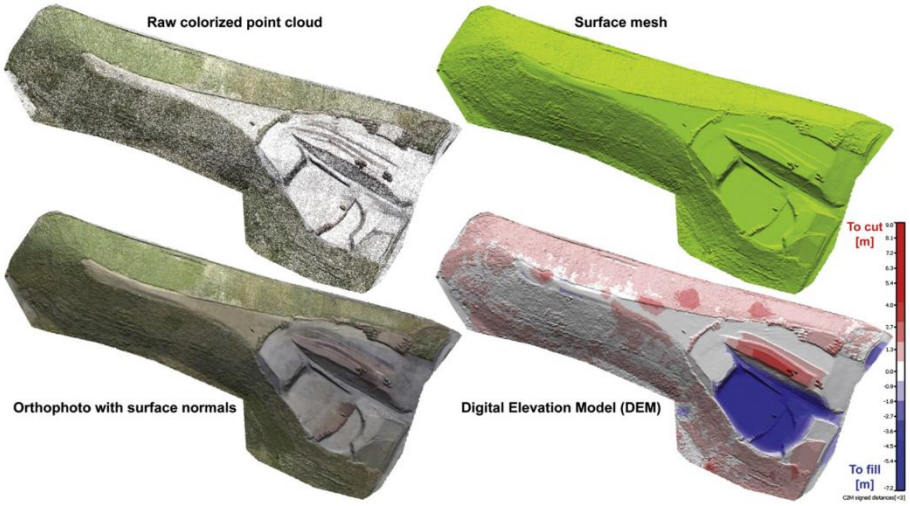

Figure 2.2 Visualization of cut-fill volume calculation from UAV-SfM

(Siebert & Teizer, 2014)

2.2.2 UAV and Laser Scanning

Another method is to use UAVs and Laser scanner. Recent research has focused on the use of UAV-SfM and Laser scanner simultaneously to obtain three-dimensional ground deformation data. Inzerillo et al. (2018) estimated the depth of surface damage based on UAV-SfM and Terrestrial Laser Scanner (TLS) at a road paving site and reflected it in the design process (Fig. 2.3). However, TLS has the disadvantage of taking a lot of time to analyze large-scale area, such as construction sites, forests. As a result, research on UAV-based Light Detection and Ranging (LiDAR) measurement, which attaches a Laser scanner to a UAV, has been conducted.

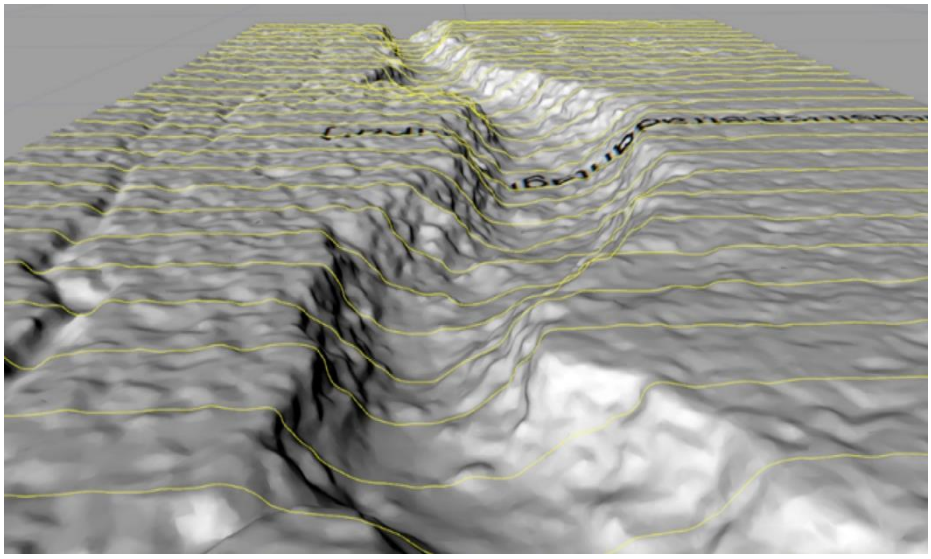

Figure 2.3 Profile curve of elevation model from UAV-SfM and TLS (Inzerillo et al., 2018)

Lee & Park (2019) conducted UAV LiDAR-based urban measurement and compared the accuracy with UAV-SfM measurement (Fig. 2.4). According to this study, it is recommended to use UAV LiDAR for large areas such as construction sites, due to its ability to monitor with high accuracy. Moreover, the automated flight capability of UAV LiDAR allows for the acquisition of high-precision 3D data without the need for field workers to understand the aircraft.

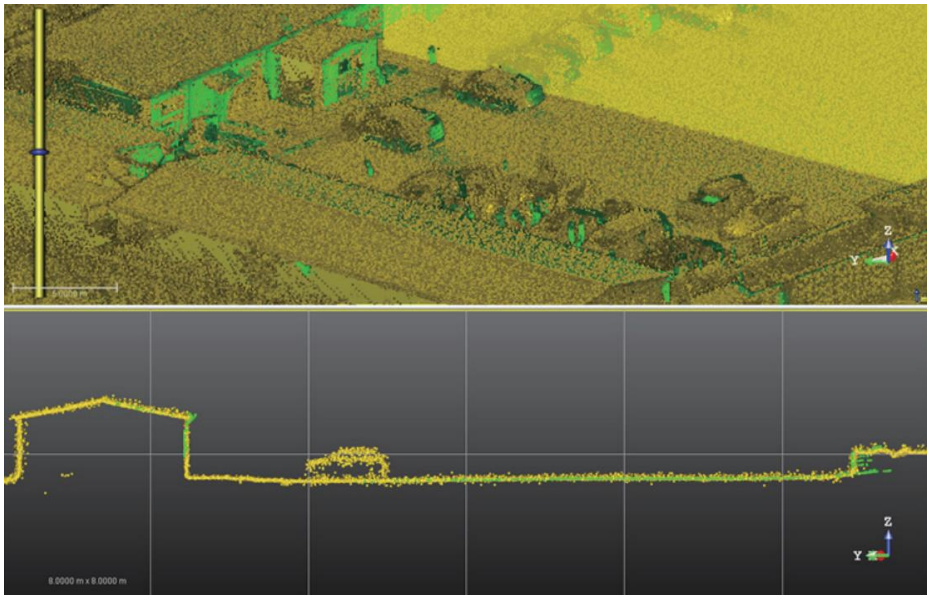

Figure 2.4 Digital surface model from UAV LiDAR (Lee & Park, 2019)

2.3 3D Point Cloud Data Processing

2.3.1 Denoising of Point Cloud Data

In particular, there is a need for research on point cloud processing techniques and parameters suitable for the construction site. SOR is an algorithm that calculates the average distance between point clouds using K-Nearest Neighbor and standard deviation. It removes point clouds that do not match the average (Han et al., 2017). MLS is an algorithm that creates arbitrary points with weights according to the importance of the data. MLS has the advantage of being able to compensate for the disadvantage of the previous noise removal algorithm, least squares method (Fleishman et al., 2005). VG is an algorithm that reduces the amount of data to remove outliers by down sampling the point cloud data (Escolano et al., 2013). Choi et al. (2022) conducted a comparative study of the denoising techniques for ground points at construction sites, yet there is no study that selects a technique that can be applied to both construction materials and ground in the construction site (Fig. 2.5).

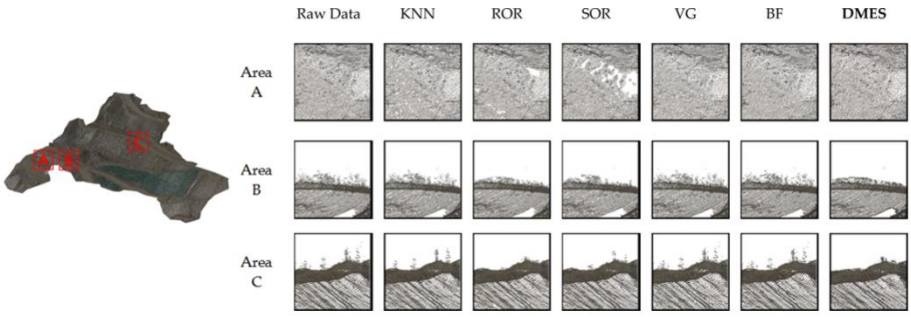

Figure 2.5 Visualization of denoising from UAV LiDAR (Choi et al., 2022)

2.3.2 Bare-earth Filtering

Yang et al. (2022) obtained bare-earth points through UAV LiDAR filtering to determine the location of the fault, emphasizing the importance of selecting a filtering technique suitable for the field. Zhang et al. (2016) demonstrated the advantages of Cloth Simulation Filtering (CSF) method for bare-earth extraction, which is applicable to various fields. It is an algorithm that classifies bare-earth points with a clothing algorithm. As the repetition progresses, 3D point clouds can be flipped up and down to obtained only bare-earth points by covering the clothing (Fig. 2.6). However, filtering parameters that can consider both bare-earth and construction materials have yet to be studied.

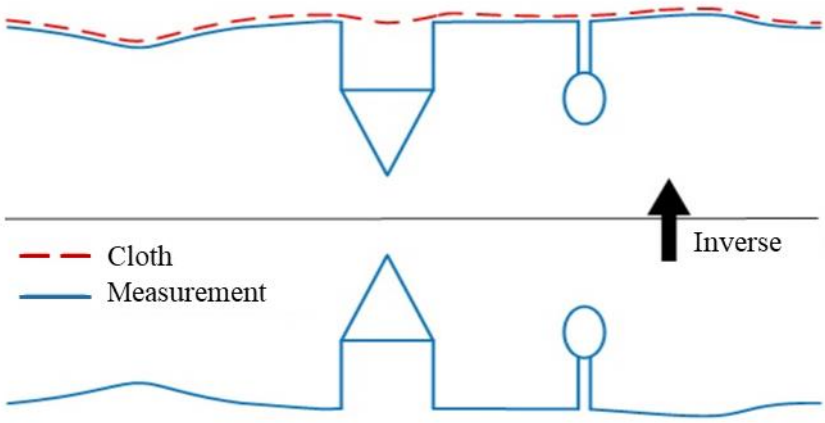

Figure 2.6 Schematic of the cloth simulation algorithm (Zhang et al., 2016)

2.3.3 Interpolation

In general, the generation of DEM from 3D point clouds of bare-earth points requires the determination of a grid size and the subsequent interpolation. The information loss resulting from the rasterization process can have a significant impact on the accuracy of the DEM. Previous studies mainly generated DEM by arbitrarily setting the grid size (Lin et al., 2019). Despite the importance of determining the optimal grid, research in this field has been lacking.

2.4 Analysis of Consolidation Settlement

2.4.1 Mapping of Settlement Rate

Previous studies have utilized UAV measurements to construct DoDs and analyze annual settlement trends. Rauhala et al. (2017) visualized the settlement occurring annually using DoDs and statistically analyzed the settlement distribution over the entire area (Fig. 2.7). They emphasized the need for research on parameters in the 3D point cloud processing stage to improve the accuracy of UAV measurements.

Moreover, several studies have analyzed long-term ground settlement through satellite measurements. These studies compared various processing methods based on different types of satellite radar. Hu et al. (2017) analyzed annual vertical and horizontal displacement of a tailing impoundment site (Fig. 2.8) using Interferometric Synthetic Aperture Radar (InSAR) and classified it into immediate settlement, primary consolidation, and secondary compression. Zhang et al. (2019) utilized persistent scatter (PS) and distributed scatter (DS)

techniques to estimate annual vertical settlement and visualize it for the management of excessive settlement-prone areas.

Previous studies mainly focused on settlement analysis in inland areas or completed construction sites with minimal settlement. Consequently, research analyzing settlement trends over large areas with low precision was predominantly conducted. However, in the case of construction sites on reclamation land, where consolidation settlement occurs, high-resolution settlement studies are needed. These studies are crucial as they can contribute to decisions regarding the timing of fill removal. Unfortunately, research on consolidation settlement using UAV measurement is still relatively limited.

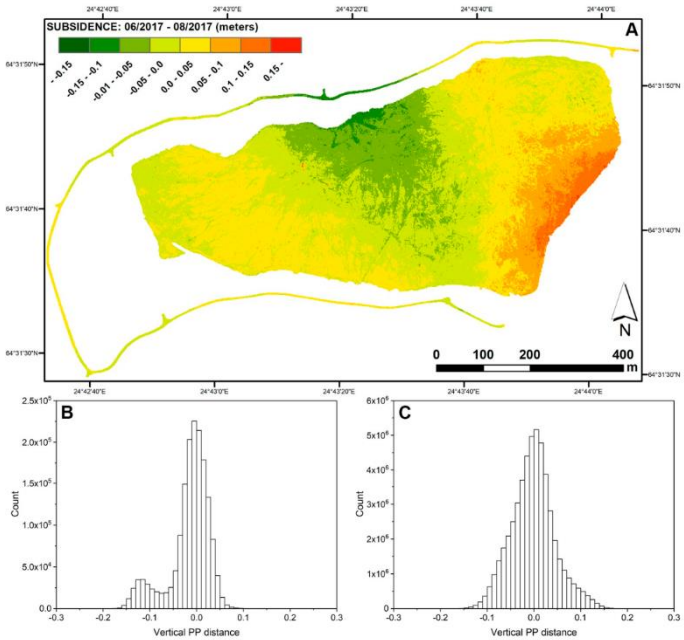

Figure 2.7 Visualization of annual settlement rate from UAV-SfM (Rauhala et al., 2017)

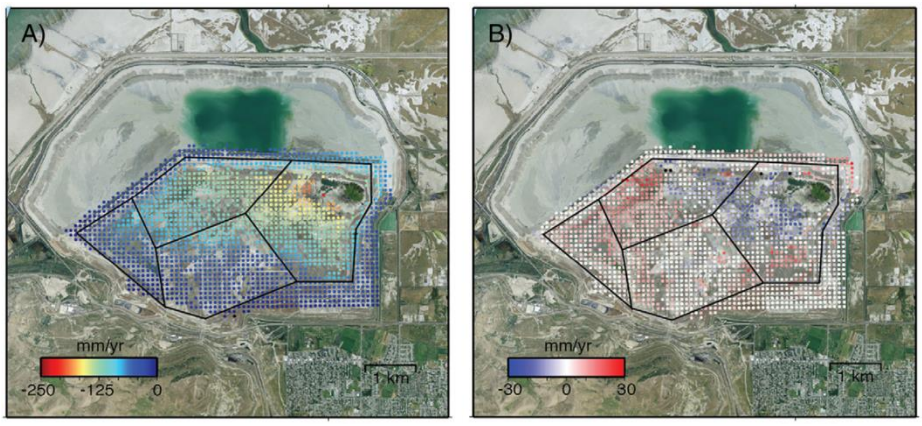

Figure 2.8 Visualization of annual vertical and horizontal displacement from InSAR (Hue et al., 2017)

2.4.2 Settlement Prediction

To precisely simulate the settlement behavior on site, a technology that can measure a wide range of construction sites in a short time and obtain high resolution data for the entire site is required. This technology should be less affected by weather conditions and cost-effective compared to existing methods. Furthermore, it should be able to secure the accuracy of settlement measurement while considering the characteristics of construction sites such as construction materials. There have been studies on settlement prediction for post-construction analysis on reclamation land. Yu et al. (2021) performed settlement prediction based on the hyperbolic method (Fig. 2.9) using measurement data obtained through small baseline subset (SBAS) InSAR and estimated the cumulative settlement and degree of consolidation. However, research on monitoring ground settlement and conducting settlement prediction using UAV during construction is still lacking.

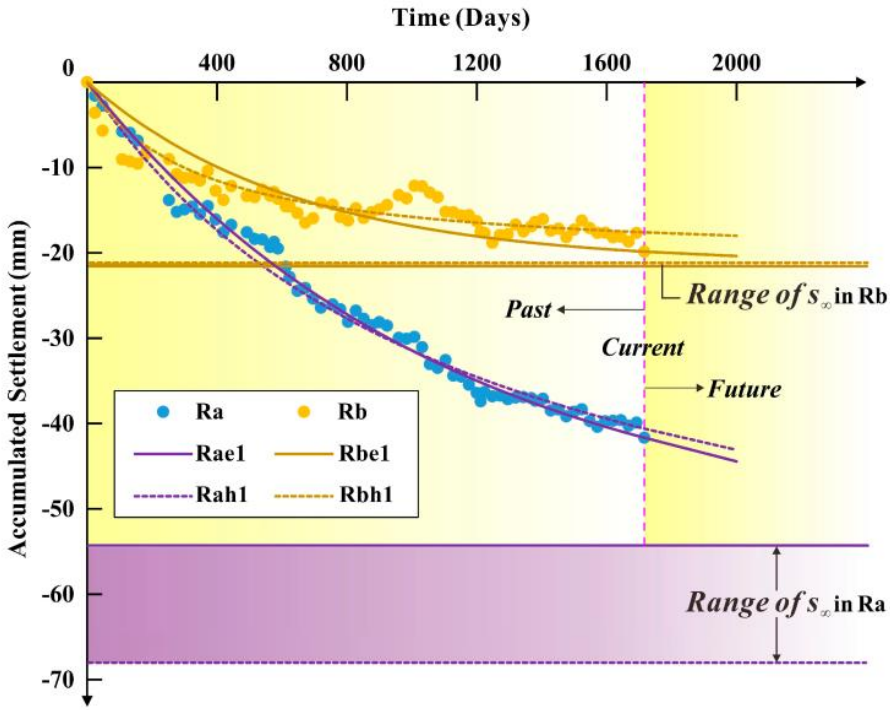

Figure 2.9 The predicted settlement based on hyperbolic and three-point modified exponential method from InSAR (Yu et al., 2021)

2.5 Summary

Numerous studies exist on UAV-based ground settlement analysis. It has been observed that achieving high accuracy for large areas is challenging through UAV photogrammetry-based studies. Therefore, for the wide construction site in this study, a combination of UAV and LiDAR measurements was deemed necessary. Additionally, the importance of studying optimal parameters for analyzing 3D point clouds obtained through UAV measurements was emphasized. Consequently, in this study, the selection of optimal parameters suitable for each point cloud analysis stage is necessary. Furthermore, while previous studies analyzed annual settlement using DEMs, it is anticipated that constructing high-resolution DEMs through UAV LiDAR measurements would ensure higher accuracy.

Chapter 3 Study Site and Measurements

3.1 Study Site

3.1.1 Overview of Busan Newport

The port of Busan located in the southeast of South Korea is responsible for most of the port traffic in the country. However, the existing port is in a state of saturation due to chronic cargo congestion, and the facilities are in a state of decline. In order to disperse the traffic and attract the transit cargo of the trunk route, the Busan Newport has been currently under construction since 1997. The Busan Newport is divided into three sections: North, South and West Container. The North Container has been completed, the South Container has been partially completed and opened, and the West Container is under construction. Fig. 3.1 shows the construction site of the West Container, which has an area of 521,700m^2. Since the Busan Newport was filled by dredged soil, the ground improvement method was applied to secure enough shear strength for the structure construction. Generally, the dredged filled construction site is left for several years after filling to allow the consolidation to be sufficiently expressed (Shi et al., 2019). The study site had passed about one year after filling. The ground improvement methods such as preloading, prefabricated vertical drains (PVDs), vacuum consolidation, and deep cement mixing (DCM) were applied to reinforce the construction site. In particular, the preloading method is the simplest and most economical method to reduce settlement and improve the bearing capacity of the soft soil (Sakleshpur et al., 2018). The

preloading method was planned with a three to four staged loading and the maximum surcharge fill was up to about ten meters height. The target area was selected based on the area with preloading method applied as shown in the Fig. 3.1.

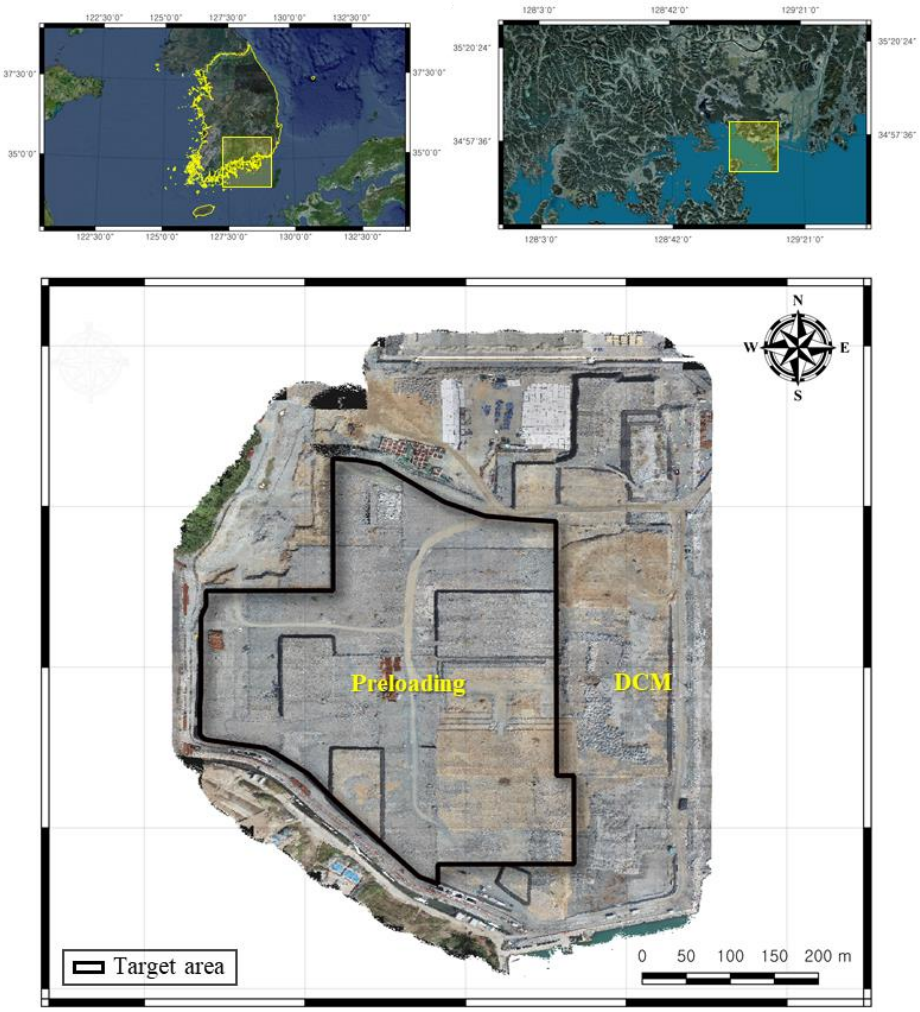

Figure 3.1 Location of the study site

The Nakdong River estuary where Busan Port is located is widely known as a weakly cohesive soil, also known as Busan, Kimhae, and Yangsan soils (Chung et al., 2002). This has led to many studies on the geotechnical characteristics of the soil (Choo et al., 2016; Suneel et al., 2008). It is important to estimate the thickness of the weakly cohesive soil layer through geophysical surveys and experiments, and to understand the compressibility and permeability characteristics. The construction period may be further extended due to the low permeability characteristics of Busan soil. In particular, in the case of a dredged soil, there are potential risks due to excessive settlement during the construction period.

3.1.2 Geotechnical Properties

Fig. 3.2 shows the soil profile and geotechnical properties of the study area. The subsurface of the site is distributed from the upper part to the sandy layer (gravel mat), the bedding soil layer, the original soil layer, the sandy layer, and the bedrock. The cohesive soil layer under the sandy layer is less than SPT-N value of ten, including the bedding soil and the original soil layer. This is evenly distributed from 5m to a maximum of 35m throughout the target site. The lower sandy layer is distributed from 35m to 50m. In addition, the bedrock was surveyed to start from 50m below the ground (Chung et al., 2007).

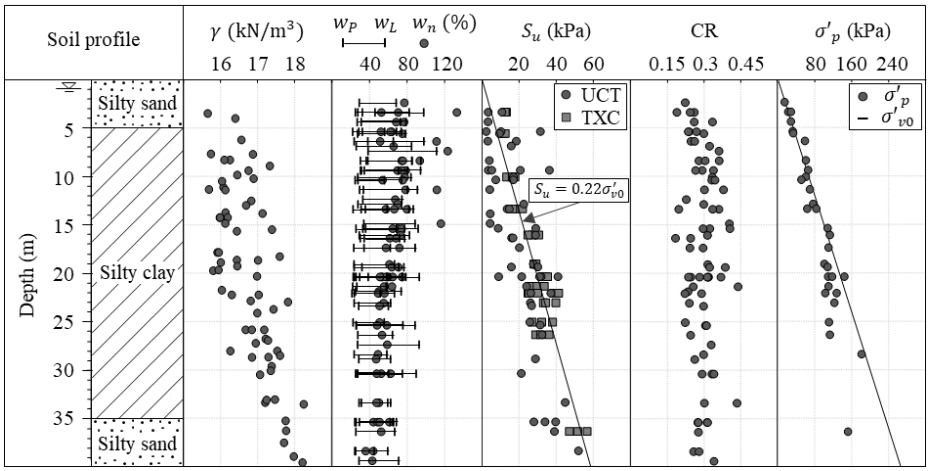

Figure 3.2 Geotechnical properties of the study site

The average unit weight of the soil layer (γ_t) was 16.23kN/m^3. The average moisture content (w_n) of the soil layer was 63.84%. It was shown that the moisture content (w_n) was located between the plastic limit (w_P) and the liquid limit (w_L). The undrained shear strength (S_u) was evaluated at different depths through uniaxial compression tests (UCT) and triaxial compression tests (TXC). It showed that the undrained shear strength has a linear relationship with depth. Additionally, the undrained shear strength showed a relationship of approximately $0.22\sigma_v'$ with the pre-consolidation pressure, indicating that it was similar to normally consolidated soil (NC). The compression ratio (CR) showed a relationship between the initial void ratio (e_0) and the compression index (C_c), which were obtained through the consolidation tests. The compression ratio varied from 0.15 to 0.45 at the study site, indicating that the soil was in a highly compressible state (Coduto et al., 2011). The pre-consolidation pressure (σ_p') determined by the consolidation tests was lower than the vertical effective stress

(σ_v'). The relationship between these two values indicated that the soil layer was in a normally consolidated state prior to construction.

3.2 Measurements

3.2.1 UAV LiDAR

Fig. 3.3(a) illustrates the UAV LiDAR used in this study. UAV LiDAR measurement was conducted 19 times at bi-weekly intervals from May 2021 to March 2022. LiDAR transmits light to objects in form of lasers and obtain the returned signal to derive the distance (USACE, 2021). Due to snow and rain, measurements were not taken, as errors could occur due to water on the ground. Point cloud is a set of points measured through LiDAR. Surface of an object can be obtained by connecting the point cloud. For the UAV LiDAR equipment, the UAV was a DJI M600, the GNSS/INS equipment was an Applanix 15, and the LiDAR was a Velodyne Puck VLP-16. The UAV moved at 5m/s and the shooting altitude was set to approximately 60m considering the height of the nearby hill. For UAV LiDAR, RTK was applied to reduce errors caused by GPS by real-time correction, so no correction was performed through GCP. Due to the limitation of the UAV battery, one measurement was divided into four sections. In some parts of the site, objects such as construction materials were present, so triple reflection was applied to acquire the data from the bare-earth as much as possible. Through the DJI Terra program, four measurement data were merged into one to obtain 3D point cloud data of the entire site. The UAV LiDAR coordinates were converted to latitude and longitude by ellipsoid (WGS84) and coordinate system (Eastern Origin) correction. UAV LiDAR data

is generally expressed in ellipsoid height, so the height was corrected by calculating the geoid height based on the Korean National Geoid Model 2018 (KNGeoid18) for the external points of the research site.

(a) UAV LiDAR

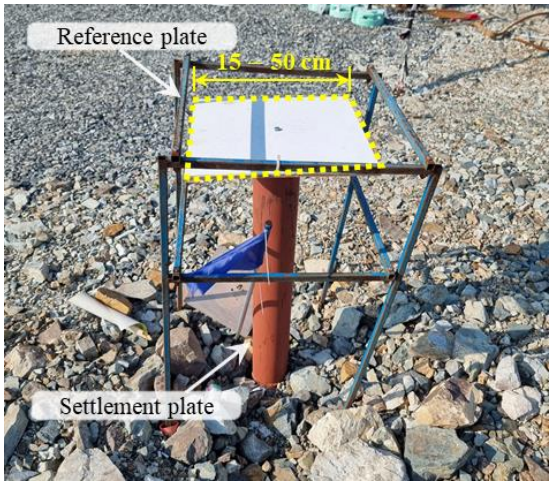

(b) Settlement plate

Figure 3.3 Instrumentations used in this study

3.2.2 Settlement Plate

Fig. 3.3(b) depicts the settlement plate used this study. The settlement plates installed on the site cover an area of approximately 10,400m^2 each, indicating that relatively few instrumentations are used compared to a large area. In this study, settlement plates were selected to identify the consolidation settlement during the preloading and to determine the timing of fill removal. Only 15 settlement plates located inside the target area where preloading was applied were selected out of the 50 settlement plates installed across the entire site. From January 2020 to March 2022, the settlement was measured through the total station at intervals of one to three days at the settlement plates. The daily measurement data showed a significant difference between the settlement plates, with 50 data points, and the UAV LiDAR, which provided approximately 100 million data points, indicating a substantial contrast in data volume.

3.3 Summary

This study was conducted at the preloading site in Busan Newport, Republic of Korea. Busan Newport exhibits similar characteristics to the representative Busan clay layer in the Nakdong River estuary. Settlement plates were installed at the study site to measure the consolidation settlement induced by preloading. In addition, UAV LiDAR measurements were performed at a two-week interval for a total of 19 measurements to monitor the settlement.

Chapter 4 Data Processing of 3D Point Cloud

4.1 Pre-processing

4.1.1 Methodology

Fig. 4.1 represents the flowchart for this study. The 3D point cloud data processing process of this study is composed of three main steps; denoising, grid analysis through interpolation, and bare-earth filtering. The accuracy of three denoising techniques were compared on three different conditions. Three representative conditions that show the characteristics of the construction site were selected: flat ground; construction material; and slope ground. Denoising was performed through Cloudcompare, and the results were compared with reference points made through Globalmapper. In this study, two indices were used to compare the results of denoising; average angle of normal vector differences and average point-to-point distances (Han et al., 2017). The formula for calculating the angle of normal vectors is as follows (Equation 4.1):

$$\theta = \cos^{-1}\left(\frac{v_1 \cdot v_2}{\|v_1\| \, \|v_2\|}\right) \qquad \text{(Eq. 4.1)}$$

Where v_1 represents the normal vector of the point after denoising, and v_2 represents the normal vector of the ground truth point. Denoising techniques used are Statistical Outlier Removal (SOR), Moving Least Square (MLS) and Voxel Grid (VG).

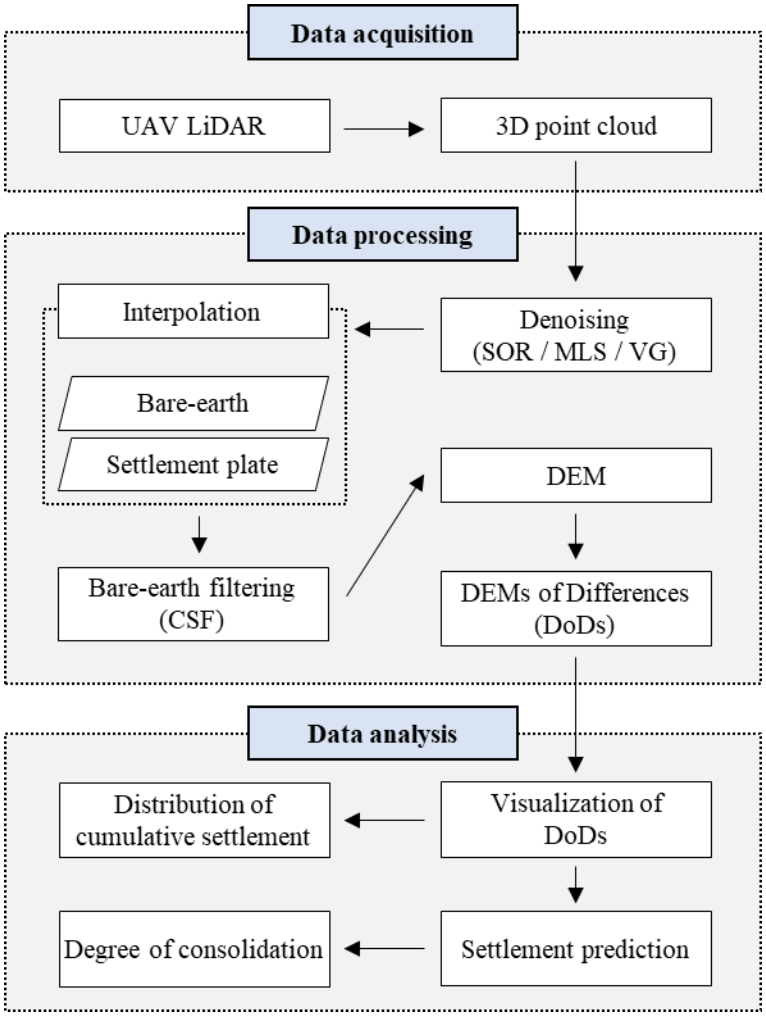

Figure 4.1 Flowchart of settlement monitoring through UAV LiDAR

4.1.2 Correction of Geoid Height

Through UAV LiDAR, three-dimensional measurement data with ellipsoid geometry was obtained. The results of converting the coordinates of the six outer points by KNGeoid18 showed an average value of 29.18m with a deviation of 1mm. In this study, the average geoid was applied uniformly.

4.1.3 Comparison of Denoising Methods

Fig. 4.2 shows the point cloud results of applying the denoising technique to three representative areas. Fig. 4.2(a-c) shows the point cloud before denoising in the flat ground, construction materials, and slope ground. Fig. 4.2(d-f) shows the result after denoising the outliers through the SOR method. As a result of the denoising, it can be seen that the point density greatly decreased in all three areas. In addition, the amount of inclined area was shown in the order of flat ground, construction materials, slope ground, which was in proportion to the decrease in point density.

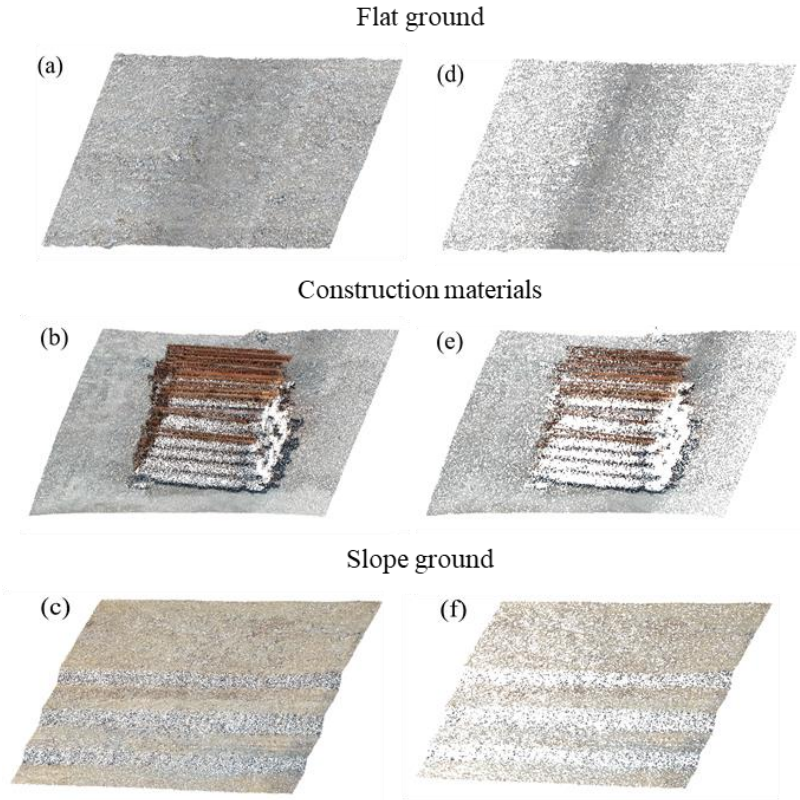

Figure 4.2 Point cloud results according to denoising method on various conditions: (a-c) raw data; (d-f) denoised data;

Fig. 4.3 and Table 4.1 show the normal vector and distance error according to denoising methods on various conditions. Fig. 4.3(a) illustrates the average angle between the normal vectors of the points before and after the denoising. Among the three methods, MLS showed a relatively large error in the slope area compared to SOR and VG. Fig. 4.3(b) depicts the average distance between the points before and after the denoising. It appears that each method does not significantly affect the results. Among three methods, the error showed a relatively large tendency in the order of flat ground, construction materials, slope ground, but the range of error was not large. When comparing the results of the three methods applied to the slope area, the errors were observed to increase in the order of SOR, VG, and MLS. Although SOR and VG yielded approximately the same results, VG resampled the points, so the study was conducted through SOR.

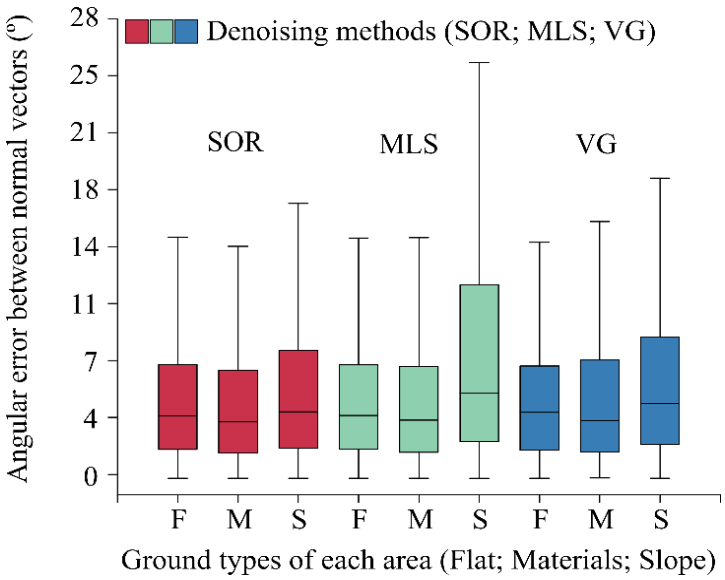

(a) Angular error between normal vectors based on various conditions

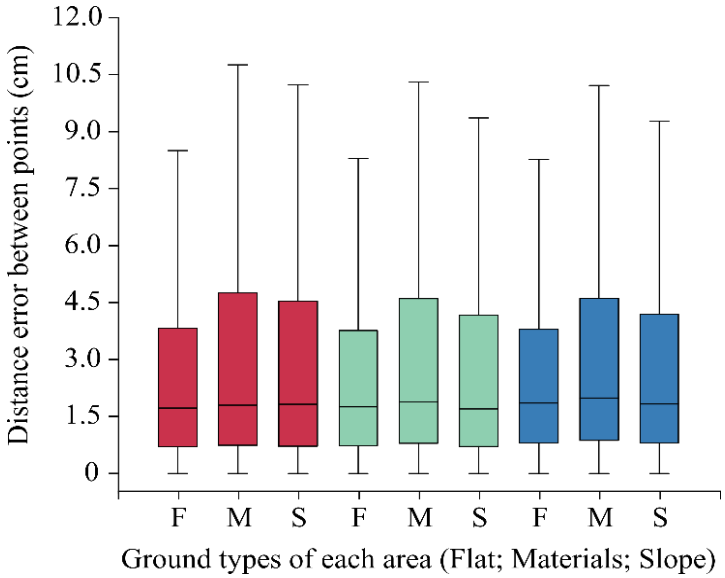

(b) Distance error between points based on various conditions

Figure 4.3 Normal vector and distance error according to denoising methods on various conditions

Table 4.1 Normal vector and distance error according to denoising methods on various conditions

Condition	Error	SOR	MLS	VG
Flat ground	θ (°)	7.5	7.3	8.2
	D (cm)	2.6	2.6	2.7
Construction materials	θ (°)	7.1	7.6	8.1
	D (cm)	7.6	7.2	7.1
Slope ground	θ (°)	8.4	13.4	9.8
	D (cm)	3.1	2.9	3.0

4.2 Interpolation

4.2.1 Methodology

It is important to select the optimal grid for constructing a DEM. In this study, the optimal grid was selected through interpolation on the bare-earth and settlement plate. This study was planned to select a suitable grid size for DEM of the site, which was preloaded with backfill gravel with maximum diameter of 30cm. On November 10, 2021, a total of 301 reference points were measured at 10cm intervals in three sections for verification. Next, it was planned to select the optimal grid at the settlement plate, but the rod of settlement plate with a diameter of 13cm did not obtain enough points for comparison. Thus, a reference plate located at top of the settlement plate was made in order to obtain enough points for selecting the optimal grid. The optimal size of the reference plate was determined by increasing the size of the plate. After installing the reference plate with optimal size, the optimal grid was then compared from 15 settlement plate. MAE was used to compare intuitively according to the grid, and RMSE was used to reduce the impact of large outlier values.

4.2.2 Interpolation on Bare-earth

In this study, the elevation of bare-earth covered with backfill gravel was validated according to the grid for comparison of accuracy. The accuracy of the UAV LiDAR-based ground elevation and the ground truth elevation was compared by increasing the grid size from 10cm to 50cm in increments of 10cm. Here, the average value of points within the grid was used to construct the DEM. Fig. 4.4 and Table 4.2 depict the measurement error on bare-earth through

RMSE and MAE according to the grid size. Since the analysis was performed on gravel-filled bare-earth with a small elevation difference, it was possible to confirm that the error range was small. According to the comparison of RMSE and MAE, it was confirmed that the accuracy was excellent for the 10cm to 50cm grid. For the 10cm to 50cm grid, the average RMSE was 2.2cm and the average MAE was 1.8cm. When it became larger than 60cm grid, a tendency of increasing error was shown. In the case of 60cm to 90cm grid, the average RMSE was 2.7cm and the average MAE was 2.1cm.

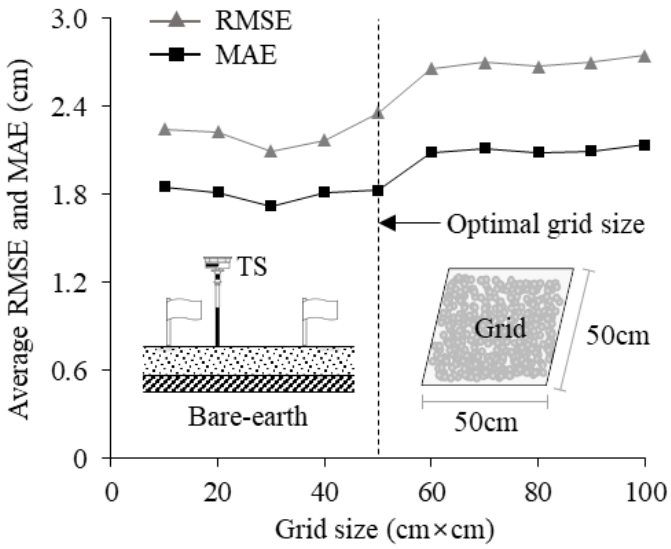

Figure 4.4 Measurement error on bare-earth according to grid size

Table 4.2 Measurement error on bare-earth according to grid size

Error metrics	Grid size (cm)				
	10×10	30×30	50×50	70×70	90×90
Average RMSE (cm)	2.2	2.1	2.4	2.7	2.7
Average MAE (cm)	1.9	1.7	1.8	2.1	2.1

4.2.3 Interpolation on Settlement Plate

The same method was used to analyze the accuracy on the settlement plate according to the grid size. Fig. 4.5 illustrates the schematic of the reference plate installed on the settlement plate in the left, and the point cloud results of settlement plate in the right. As shown in the right figure, it can be seen that the points are distributed discretely when the point cloud is enlarged. The diameter of the settlement plate at the study site was 13cm, so the reference plate with lengths of 15cm, 20cm, 30cm, 40cm, and 50cm were respectively installed. When the size of reference plate was over 50cm×50cm, it exceeded the size of the fence installed around the settlement pile, so it was determined as the maximum size. The reference plate was coated so that it would not be affected by rain, and it was made white for easy reflection by LiDAR. The point density obtained by UAV LiDAR measurement was compared by installing different sizes of reference plates. Table 4.3 shows the point density on the reference plate according to the top plate size. The point density was 5pt/m^2 in the 15cm×15cm reference plate, and it showed an exponential growth trend as the size increased. Thus, 50cm×50cm was selected as the appropriate reference plate that obtains the maximum precision of 32pt/m^2.

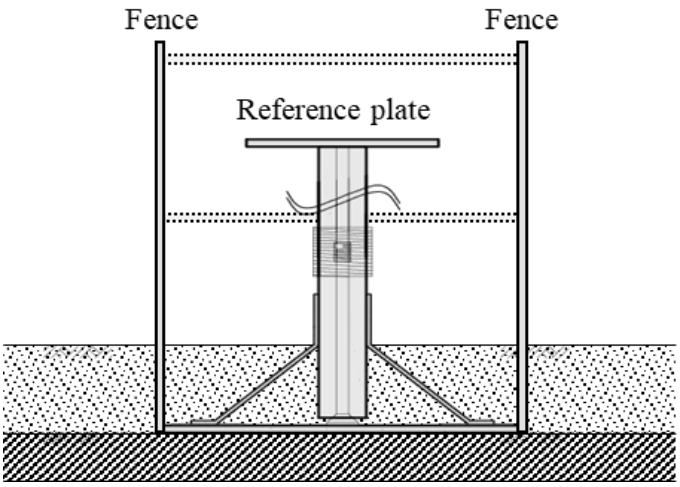

(a) Schematic of settlement plate

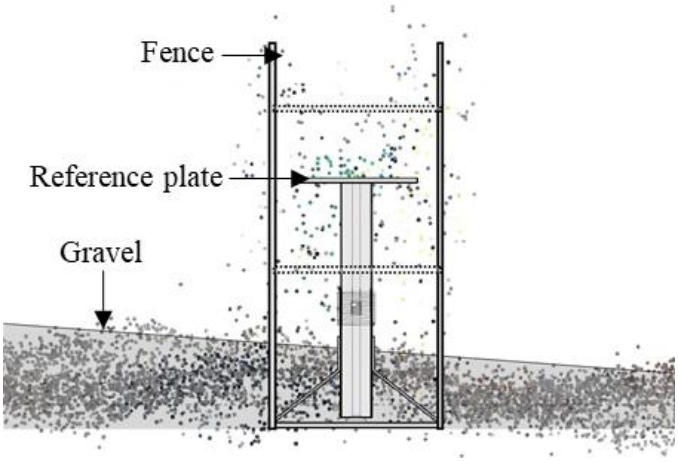

(b) Point cloud results

Figure 4.5 Point cloud results on settlement plate

Table 4.3 Point density on reference plate

Grid size (cm)	15×15	20×20	30×30	40×40	50×50
Point density (pts/cm^2)	5	7	13	21	32

On November 10th, 2021, 15 settlement plates with a 50cm×50cm reference plate were used for selecting the optimal grid size of settlement plate. 15cm, 20cm, 30cm, 40cm, and 50cm grid were compared to manual measurement data. When the grid size exceeded 50cm, it overestimated the ground level and error greatly increased due to the fence level. The error may occur due to the fact that some settlement plates had tilted during the gravel filling process up to maximum 10m, causing the reference plate to tilt as well. Fig. 4.6 and Table 4.4 show the measurement error on settlement plate through RMSE and MAE according to the grid size. In the case of 15cm to 20cm grid, the average RMSE was 23cm and the average MAE was 16cm. In the case of 30cm to 50cm grid, the average RMSE was 18cm and the average MAE was 14cm. It was judged that the use of 50cm grid was appropriate, as the efficiency of analysis time was considered. Thus, the optimal grid size for both bare-earth and settlement plate was determined to be 50cm×50cm.

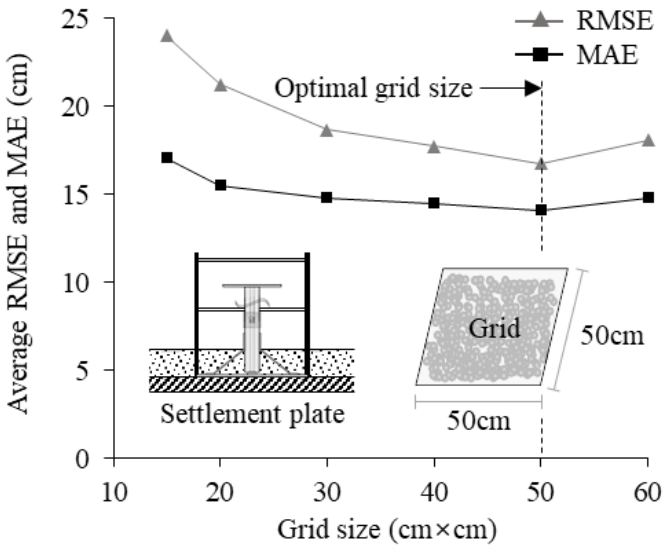

Figure 4.6 Measurement error on settlement plate according to grid size

Table 4.4 Measurement error on settlement plate according to grid size

Error metrics	Grid size (cm)				
	15×15	20×20	30×30	40×40	50×50
Average RMSE (cm)	24.0	21.2	18.7	17.7	16.7
Average MAE (cm)	17.1	15.5	14.8	14.5	14.1

Fig. 4.7 compares the cumulative settlement of UAV LiDAR-based measurement (S_{LiDAR}) and manual measurement by total station (S_{TS}) over 10 months. It was measured with 15 settlement plates in 50cm grid. As shown in the figure, the coefficient of determination in the optimal grid size was 0.967, and there was no tendency to clearly underestimate or overestimate. Even after ten months, the accuracy of the cumulative settlement of UAV LiDAR-based measurement and manual measurement were in good agreement.

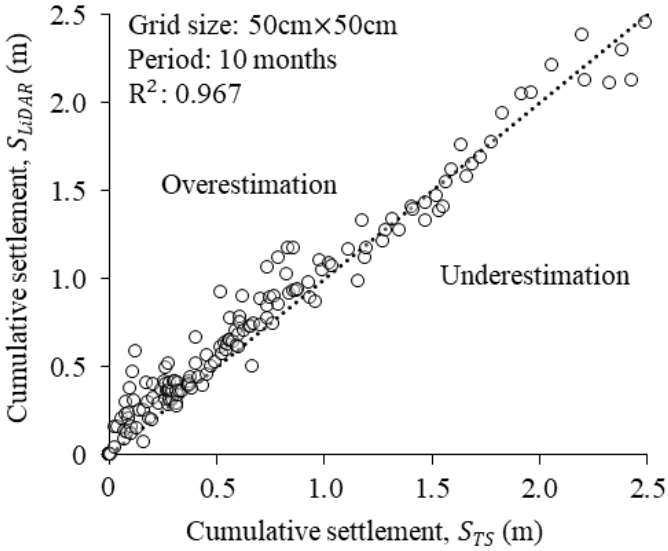

Figure 4.7 Comparison of settlement between UAV LiDAR and total station

4.3 Filtering

4.3.1 Methodology

In this study, it was necessary to create a DEM in the form of a bare-earth point in order to analyze the settlement, removing the influence of construction materials and vehicles from the UAV LiDAR measurement data. As the ground is covered by objects, UAV LiDAR scanning can be hindered due to the hidden area. Thus, bare-earth points were extracted by filtering method, and parameter optimization was performed. In this study, CSF technique, a bare-earth point filtering, was applied to remove objects on the ground. In this study, optimization was performed to derive the optimal parameters in the preloading construction site. To evaluate the filtering results quantitatively, the Cohen's kappa coefficient (k) was used. The formula for calculating the Cohen's kappa

coefficient is given by Equation 4.2. Equation 4.2 can be derived using Equation 4.2 and Equation 4.3:

$$p_0 = \frac{a+d}{e} \qquad \text{(Eq. 4.2)}$$

$$p_c = \frac{(a+b)\times(a+c)+(c+d)\times(b+d)}{e^2} \qquad \text{(Eq. 4.3)}$$

$$k = \frac{\mathrm{p_0} - p_c}{1-\mathrm{p_c}} \times 100\% \qquad \text{(Eq. 4.4)}$$

Where a is a point that is clearly classified as bare-earth, b is a point that is misclassified as bare-earth, c is a point that is misclassified as object, and d is a point that is correctly classified as object, and $e = a + b + c + d$. bare-earth point filtering was performed through the Cloudcompare, and the results were compared with the reference points constructed through the Globalmapper. For regions without objects, it was not possible to identify the accuracy of filtering, so the results were compared only for the construction material area.

4.3.2 Bare-earth Filtering

We obtained bare-earth point with objects removed in order to monitor the settlement. The bare-earth point filtering was applied using the CSF technique. To perform the filtering, UAV LiDAR data from November 10, 2021 was used. There are a total of six parameters for CSF, and four were set to be suitable for the site, and only two variables were changed. Since surcharge fill was performed with a maximum of ten meters high, Rigidness was set to two and Slopesmooth to True. Time step and Iteration were applied to the commonly

used values of 0.65 and 500, respectively. Zhang et al. (2016) proposed to find parameters suitable for the site by changing the Threshold*(h_{cc})* and Grid resolution*(GR)*. Accordingly, the Threshold was increased by 0.05 intervals within the range of 0.01 to 0.3, and the Grid resolution was increased by 0.5 intervals within the range of 0.1 to 3.5. If the Threshold was less than 0.01, no filtering was performed on any object, and if the Grid resolution was greater than 3.5, the surcharge fill was recognized as an object, so the range of parameters was determined.

In this study, the filtering accuracy was compared through the Cohen's kappa coefficient for 56 cases. Fig. 4.8 shows the results of filtering through CSF. The filtering is generally considered to be accurate when the Cohen's kappa coefficient is above 0.8. It was also shown that the Cohen's kappa coefficient was distributed over a wide range from a minimum of 0.087 to a maximum of 0.906. Fig. 4.8(a) shows the result of the parameter combination with the highest accuracy (k = 0.906), where construction materials are clearly classified. On the other hand, Fig. 4.8(b) shows the result of the parameter combination with the lowest accuracy (k = 0.087), where only some of the construction materials are removed. In this study, bare-earth filtering was performed with the case of highest accuracy, which showed the maximum Cohen's kappa coefficient.

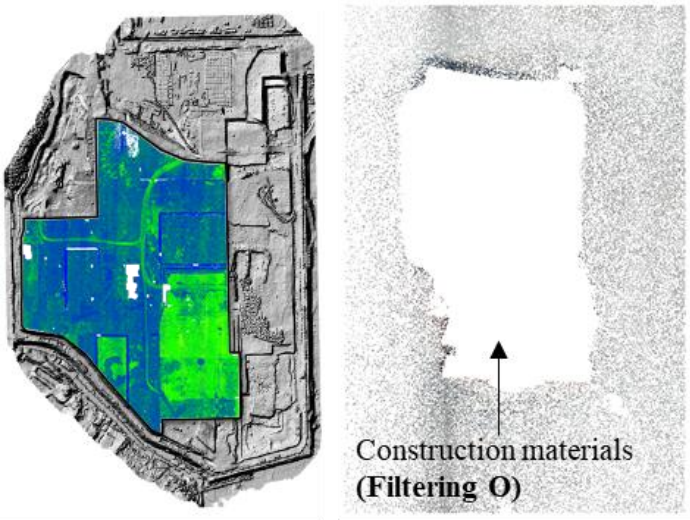

(a) h_{cc} = 0.3 and GR = 3.0

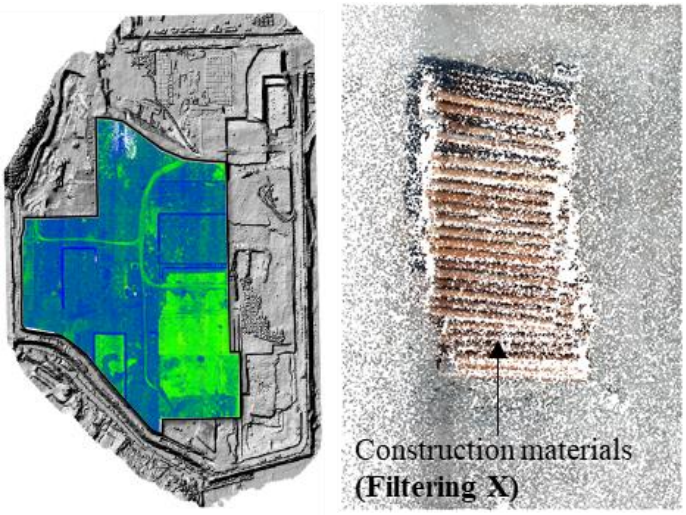

(b) h_{cc} = 0.1 and GR = 0.1

Figure 4.8 Comparison of CSF results on construction materials

4.4 Summary

In this study, data processing of 3D point cloud data was conducted through denoising, interpolation-based grid analysis, and bare-earth filtering. First of all, three denoising techniques were compared for three specific conditions, and the SOR technique was selected as the optimal method. Next, grid analysis was performed for the settlement plates and the bare-earth, resulting in the selection of a 50cm grid size as the optimal choice for the DEM. Lastly, bare-earth filtering was performed using the CSF method, and the optimal parameters were determined to construct the DEM for the entire site.

Chapter 5 Visualization of Consolidation Settlement

5.1 Methodology

In this study, DoDs were calculated to analyze the settlement rate based on the optimal grid size DEM at the study site. The monthly settlement rates were derived by differencing the monthly DEMs over a period of approximately 10 months, starting from May 2021. The raster calculator function in the QGIS program was utilized for the computation of monthly settlement rates. The distribution of monthly settlement rates was analyzed and exhibited a deviation in a normal distribution.

Furthermore, a comparison of cumulative settlement was performed based on the surrounding section size using the settlement plates as a reference. Fig. 5.1 illustrates the algorithm used in this study to determine the cumulative settlement utilizing UAV LiDAR-based measurements. Since UAV LiDAR measurements capture the surface elevation, the absolute elevation was not utilized. Instead, the relative change in the surface elevation between measurement periods was employed to estimate the settlement. Consequently, during the preloading period (t_1 to t_2) where no significant filling operation occurs, settlement can be accurately estimated without errors. However, during the filling operation period (t_2 to t_3), accurate estimation of settlement based solely on relative changes is not possible. Therefore, in this study, the settlement before the filling operation (t_1 to t_2) was used to interpolate the settlement during the soil deposition period (t_2 to t_3), enabling the calculation of cumulative settlement ($1 - 2 - 3' - 4$).

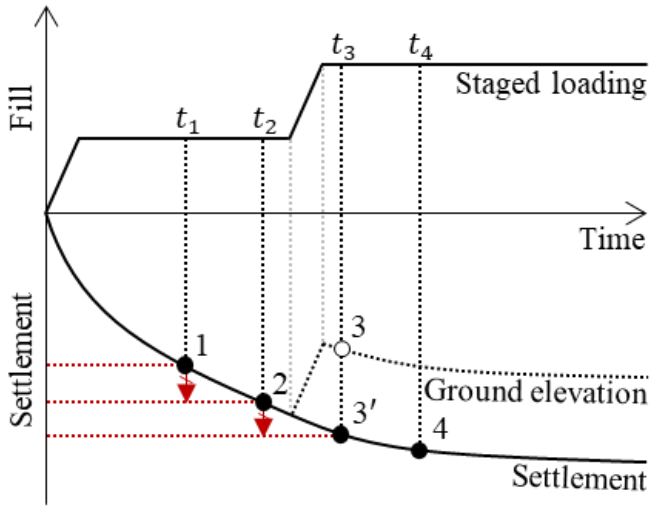

Figure 5.1 Procedure of time-series settlement data correction during staged loading

5.2 Monthly Settlement Rate

0.5m DEM was constructed at monthly intervals using a point cloud filtered by CSF. The DEM was used to obtain DoDs to visualize the monthly settlement rate of the entire site. Rauhala et al. (2017) visualized the settlement rate based on the distance of time-series point cloud, but the errors were shown due to the discrete distribution of the point cloud. In this study, the optimal DEM was used for DoDs to reduce the potential errors.

The entire site is divided into approximately 31 different fill sections, each with a different filling period. Fig. 5.2(a) shows the visualization of the monthly changes in ground elevation ($\delta_{elevation}$) on the entire section over a one-month period from October to November 2021. Here, red color indicates that the

ground level is increasing as it gets darker, which usually means sections with additional filling operated. Blue color indicates that the ground level is decreasing as it gets darker, which means sections where filling has been removed or where settlement has occurred. Visualization of the site with red and blue color was commonly used in cut-fill volume calculation (Siebert and Teizer, 2014). In order to distinguish the settlement rate from filling operation, the scale of the visualization was adjusted according to the same fill section, which is located at the right below corner. This section is at the staged loading operation, and the monthly settlement rate of the settlement plate located in this section by total station was 0.5m. Thus, it was judged that the settlement rate that exceeded 0.5m was considered as removed fill. By setting the maximum scale of blue color to 0.5m, the area where blue is displayed as a solid object with the same intensity are sections where filling is removed, and the areas where blue is displayed as a scatter are sections where settlement occurs. From the fig. 5.2(a), it can be seen that settlement is occurring because the blue shows distributed color in the same fill section. In addition, the color scale of 0.01 or less was judged to be a range where errors may occur due to vehicle vibration, and was displayed in a transparent color.

Fig. 5.2(b) shows the visualization of the monthly changes in ground elevation ($\delta_{elevation}$) over a month from January to February 2022 for the entire area. The maximum scale of blue was set to 0.5m as well as Fig. 5.2(b), and any values exceeding 0.5m were judged to be sections where filling was removed. Some sections are indicated by blue and red objects (Solid), which can be seen as sections where filling was removed or sections where soil was

re-filled, respectively. The same fill section at the bottom right is at the moment after the final loading process. In the figure, the blue is shown to be scattered dots in the same fill section, which indicates that the settlement is occurring. Compared to Fig. 5.2(a), it can be also seen that the monthly change has decreased overall.

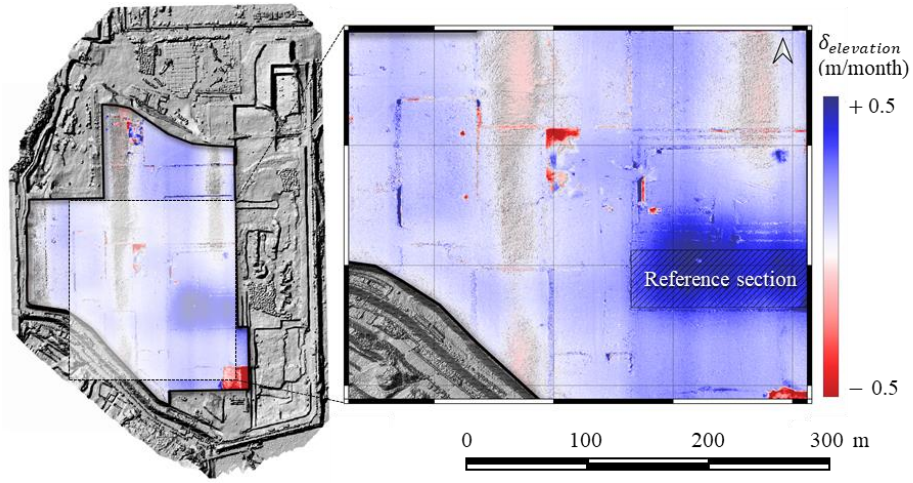

(a) October 22, 2021 - November 25, 2021 (t_1)

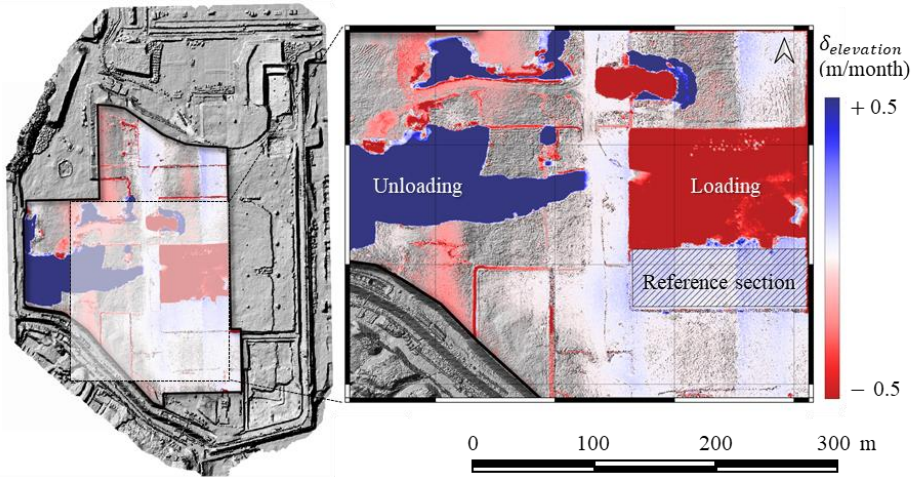

(b) January 21, 2022 - February 22, 2022 (t_2)

Figure 5.2 Visualization of monthly changes in ground elevation

Fig. 5.3 compares the distribution of monthly settlement rate in the same fill section outlined in Fig. 5.2. Kim et al. (2013) also visualized the consolidation settlement of 50m DEM using the same method. Fig. 5.3(a) is at the staged loading operation, while Fig. 5.3(b) shows the distribution after the final loading process. In order to monitor the consolidation settlement occurring in the downward direction, the color scale was set to a minimum of 0 and a maximum of 0.5m.

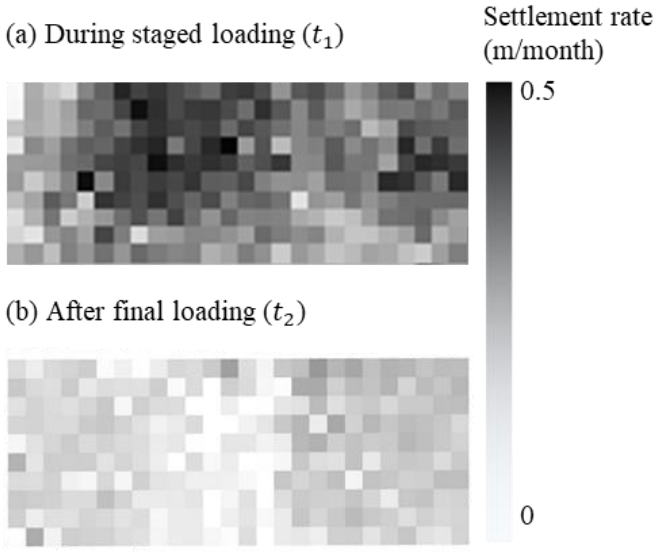

Figure 5.3 Monthly settlement rate at the reference section

Fig. 5.4 shows the distribution of monthly settlement rate at aforementioned two period represented using a bar graph. It is the same as Fig. 5.3, representing the staged loading operation (t_1) and after the final loading process (t_2). Kim et al. (2013) demonstrated the distribution of coefficient of

consolidation through the probability density function, which was represented by a bar graph for analysis. In this study, the average monthly settlement rate during the 10-month UAV LiDAR measurement period showed a general trend of decreasing by approximately 0.07m/month. The trend of the settlement rate change over a period of three months out of the 10 months. Even during construction, the average monthly settlement rate decreased overall, but it was possible to confirm that the distribution of monthly settlement rate maintained the same distribution pattern. It is in good agreement with the overall settlement rate distribution decreasing in the study by Rauhala et al. (2017). In the overall distribution of monthly settlement rate, the settlement rate measured manually at the settlement plate is strongly indicated. The monthly settlement rate at the settlement plate can be seen to decrease from t_1 to t_2. At this time, the maximum monthly settlement rate after the final settlement was up to 0.5m/month in the same settlement section. In addition, after the final loading process, the deviation of the settlement rate was up to a maximum of 0.25m per month, indicating the possibility of differential settlement.

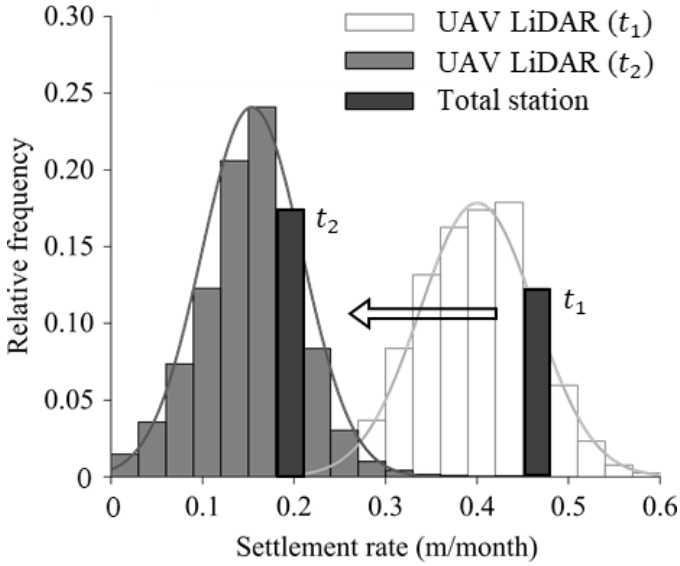

Figure 5.4 Distribution of monthly settlement rate at the reference section

5.3 Consolidation Settlement Distribution

Fig. 5.5 illustrates the results of cumulative settlement measured by UAV LiDAR over a period of 10 months at two settlement plate locations. The distribution range of settlement values resulting from UAV LiDAR measurements was determined for three different sections: 10m×10m, 50m×50m, and 100m×100m, with the settlement plate as the center. The calculation of cumulative settlement was based on the algorithm presented in Fig. 5.5, utilizing the DoDs derived from the 0.5m DEM. Kim et al. (2016) evaluated the 90% confidence interval statistically through the probability density function to analyze the settlement. In this study, the settlement measured by UAV LiDAR-based DoDs is represented as an error band within the 2σ range of the settlement distribution. Comparing the results of settlement

plate (SP-1) and UAV LiDAR measurements, it can be observed that the distribution of settlements for the 10m×10m and 50m×50m sections is similar to the settlement results obtained from the settlement plates. However, for the 100m×100m section, the settlement distribution is significantly larger, more than twice as large as the previous sections. Similarly, when comparing the settlement plate (SP-2) and UAV LiDAR measurements, a similar trend of increased settlement distribution with increasing section size was observed, as shown in SP-1. Particularly, for the 100m×100m section, the settlement distribution range was approximately twice as large as that of the 50m×50m section.

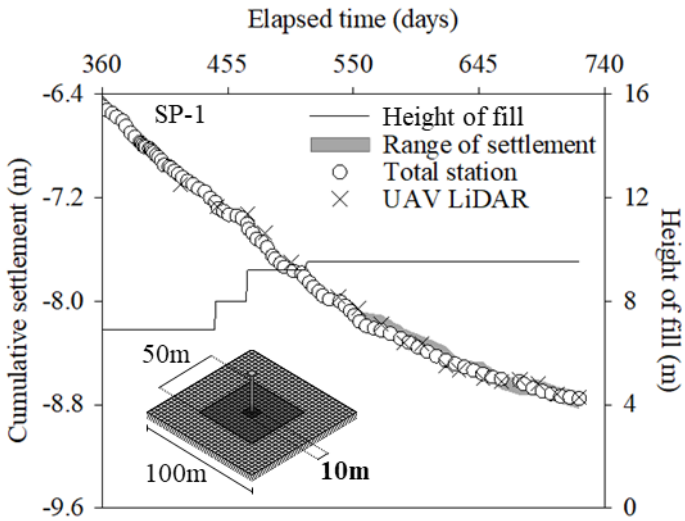

(a) Section of 10m×10m from SP-1

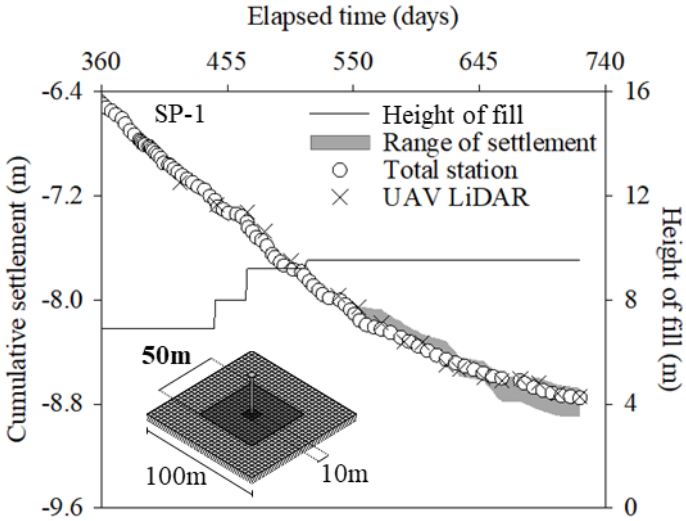

(b) Section of 50m×50m from SP-1

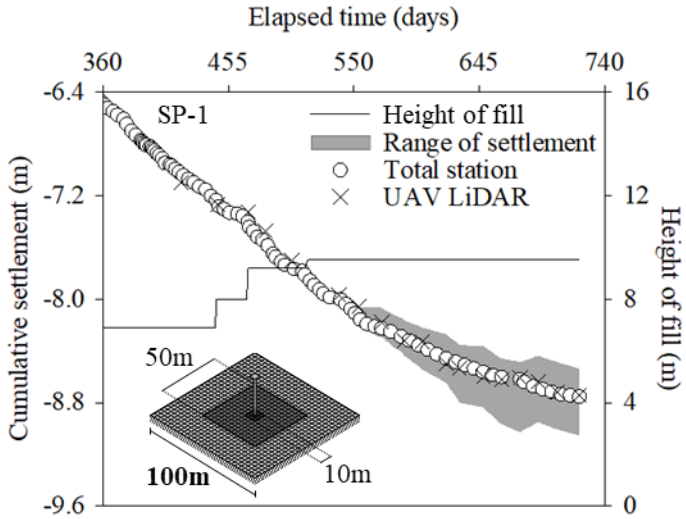

(c) Section of 100m×100m from SP-1

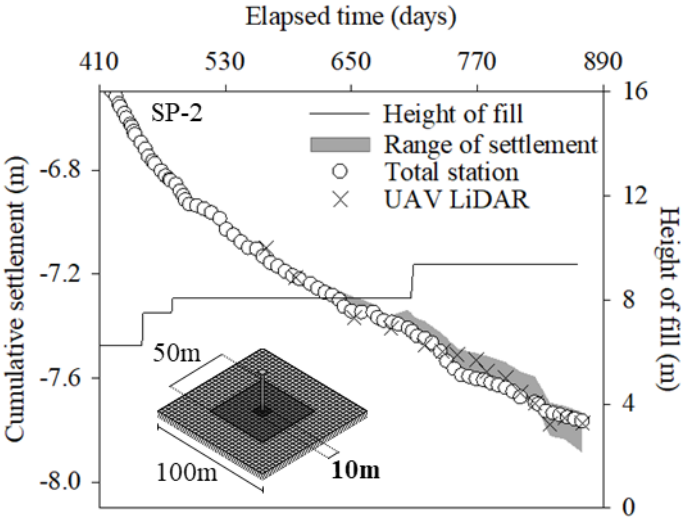

(d) Section of 10m×10m from SP-2

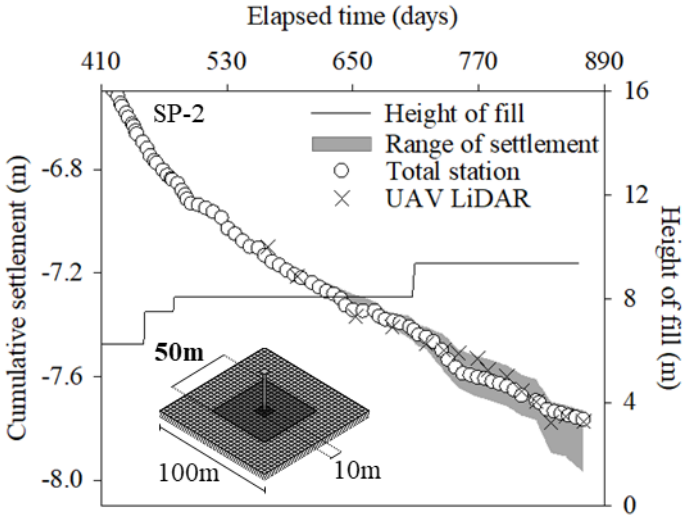

(e) Section of 50m×50m from SP-2

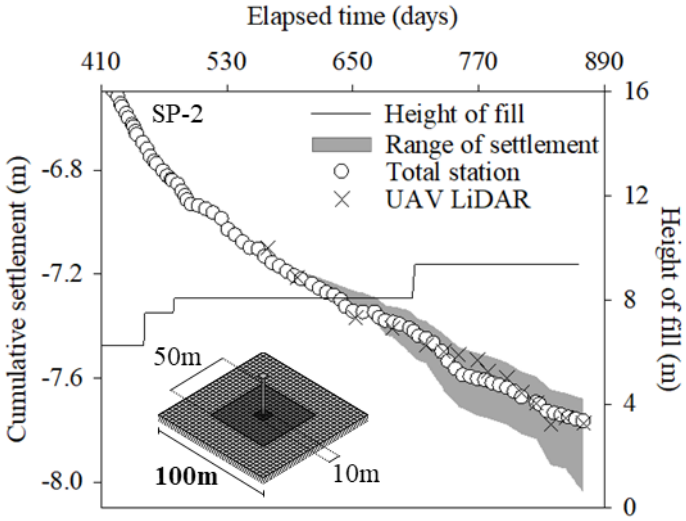

(f) Section of 100m×100m from SP-2

Figure 5.5 Cumulative settlement-time curve with range of settlement according to section size

5.4 Summary

Monthly settlement rates were analyzed and visualized for the entire site. Based on the maximum values of settlement rates for each period, the areas of settlement, filling, and cutting were delineated. Through the analysis, it was confirmed that variations in settlement rates occur even after the final loading within the same fill section. Next, an analysis of cumulative settlements was conducted, revealing significant differences in settlement distributions when managing settlement plates with a current arrangement spacing of 100m×100m. These findings highlight that the variability in settlement distribution within a 100m×100m section near the settlement plates is more than twice as large as that within a 50m×50m section. Additionally, it can be recommended to perform comprehensive settlement management by distinguishing sections with a 10m×10m.

Chapter 6 Analysis of Settlement Prediction

6.1 Methodology

In this study, the hyperbolic method-based settlement prediction was performed, and the predicted results were compared. The hyperbolic method is based on the assumption that settlement rate in the field decreases following a hyperbolic trend. By establishing a correlation between time and settlement, settlement can be predicted. For the prediction, only data after the completion of final fill are utilized, and the settlement prediction formula is represented by Equation 6.1. By modifying this formula, the final settlement can be determined, and the formula for calculating the final settlement is given by Equation 6.2. In this study, the accuracy was evaluated by comparing the final settlement, and the degree of consolidation was determined using Equation 6.2 for the analysis.

$$S = S_i \frac{t - t_i}{\alpha(t - t_i) + \beta} \qquad \text{(Eq. 6.1)}$$

$$S_f = \frac{1}{\beta} \qquad \text{(Eq. 6.2)}$$

In this study, the cumulative settlement distribution according to the section size was represented as a normal distribution, allowing the determination of the average and standard deviation of the settlement distribution. The settlement predictions based on the hyperbolic method were compared using the average settlement values calculated from the settlement distributions for each section size. Furthermore, the accuracy of settlement

prediction was analyzed based on the number of measurements. While the settlement plates were measured every few days, the UAV LiDAR measurements were conducted at relatively longer intervals of two weeks. Therefore, an analysis was performed to determine the minimum number of measurements required to achieve high prediction accuracy from the time after the completion of final fill for the settlement prediction. Finally, settlement monitoring was performed by calculating the degree of consolidation at the specific date based on the ratio between the cumulative settlement up to the date and the predicted final settlement.

6.2 Settlement Prediction by Hyperbolic Method

Fig. 6.1 shows the distribution of cumulative settlement for three different section sizes, represented as normal distributions. It was observed that the average values calculated from the settlement measurements obtained through UAV LiDAR for the three section sizes were similar to the measurements from the settlement plates. It can be observed that the deviation of the settlement distribution significantly increases in the 50m×50m section compared to the 10m×10m section. Conversely, the deviation in the 50m×50m and 100m×100m sections appeared to be similar. These findings confirm that as the size of section increases, the deviation of settlement distribution also increases while the average values remain relatively constant.

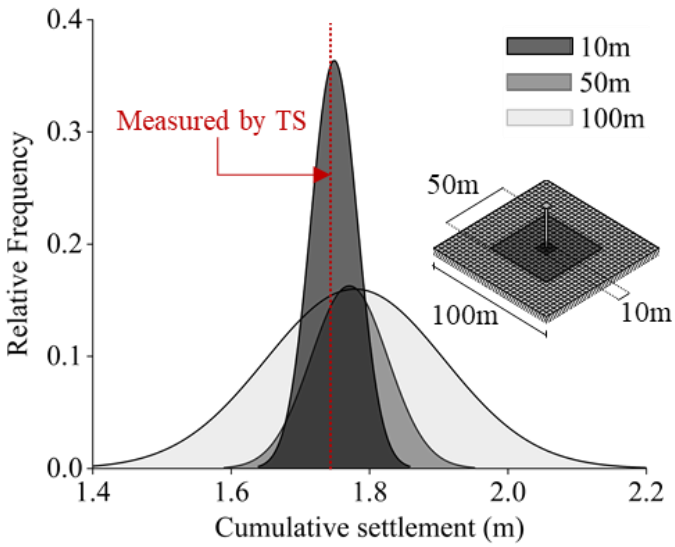

Figure 6.1 Distribution of cumulative settlement according to section size

Next, settlement predictions were performed using the average values within each section size based on the hyperbolic method. Fig. 6.2 presents the results of settlement prediction based on the UAV LiDAR measurements of settlement from three sections: 10m×10m, 50m×50m, and 100m×100m. The predicted settlement results were compared by calculating the prediction errors for the final settlement. Table 6.1 shows the prediction accuracy of final settlement according to section size. The comparison of predicted final settlement values showed an error range of 0.01 to 0.04m for the 10m×10m section, which corresponds to an error ratio of 0.08 to 0.41% of the total settlement. This indicates a high level of prediction accuracy. For the 50m×50m section, the errors were 2 to 23 times larger compared to the 10m×10m section, with error ratios ranging from 2 to 34 times larger. Similarly, for the

100m×100m section, the errors were 6 to 36 times larger compared to the 10m×10m section, with error ratios ranging from 6 to 53 times larger. The comparison of the three section sizes indicated that as the area increased, the prediction errors significantly increased. Therefore, it was determined that performing settlement prediction using a 10m×10m section size would be desirable.

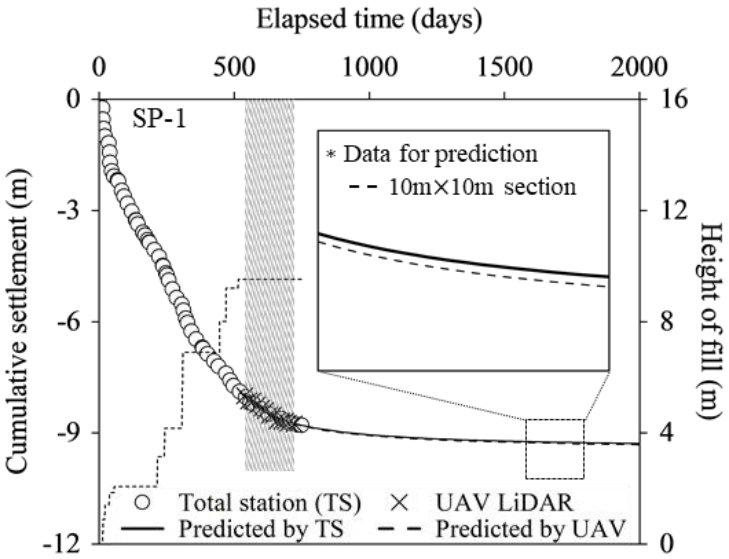

(a) Section of 10m×10m from SP-1

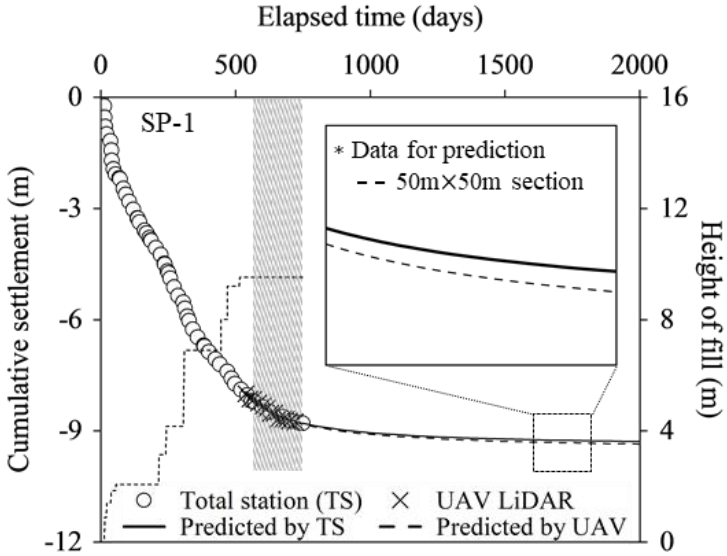

(b) Section of 50m×50m from SP-1

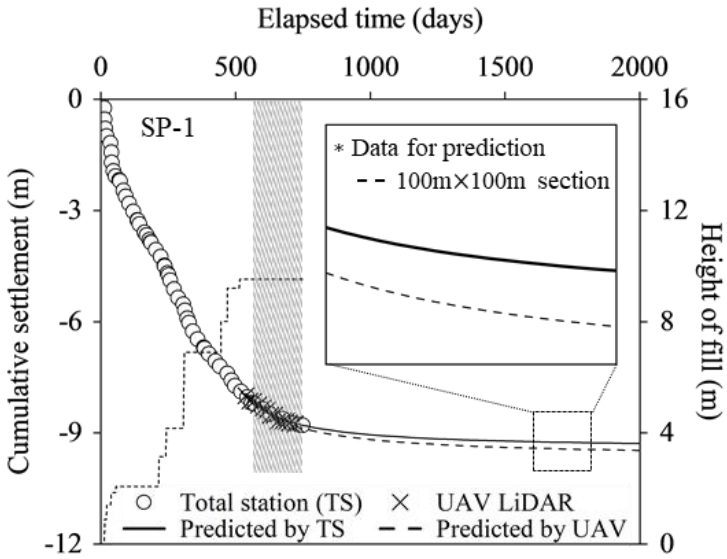

(c) Section of 100m×100m from SP-1

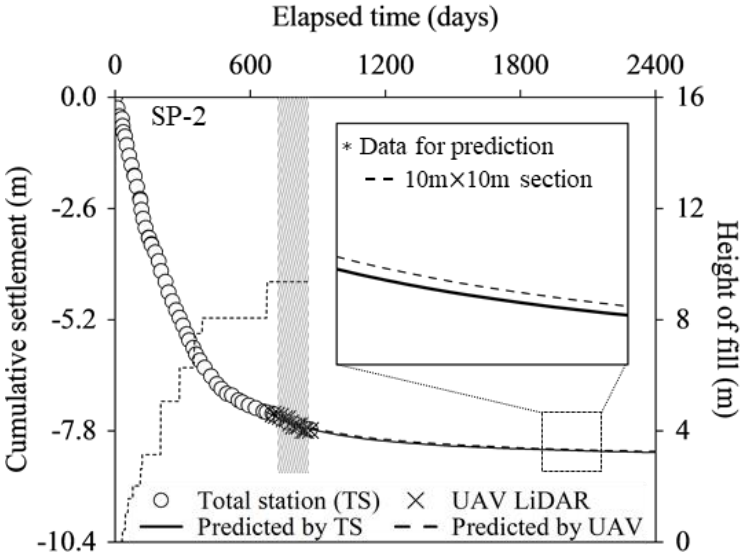

(d) Section of 10m×10m from SP-2

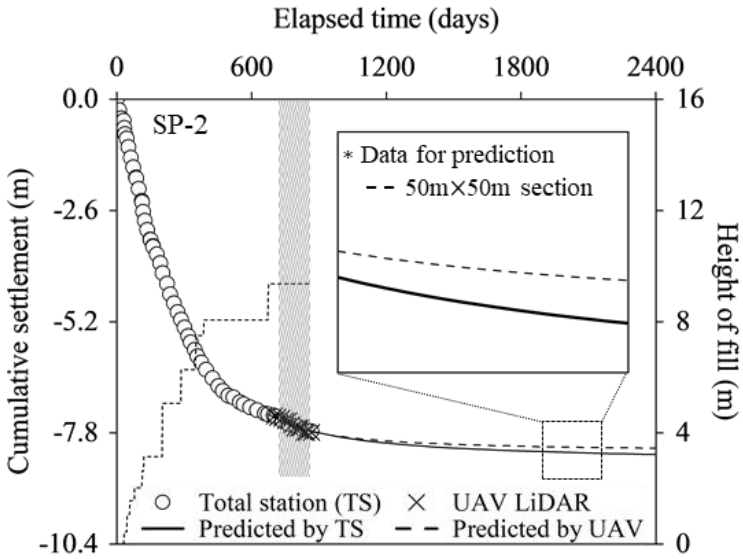

(e) Section of 50m×50m from SP-2

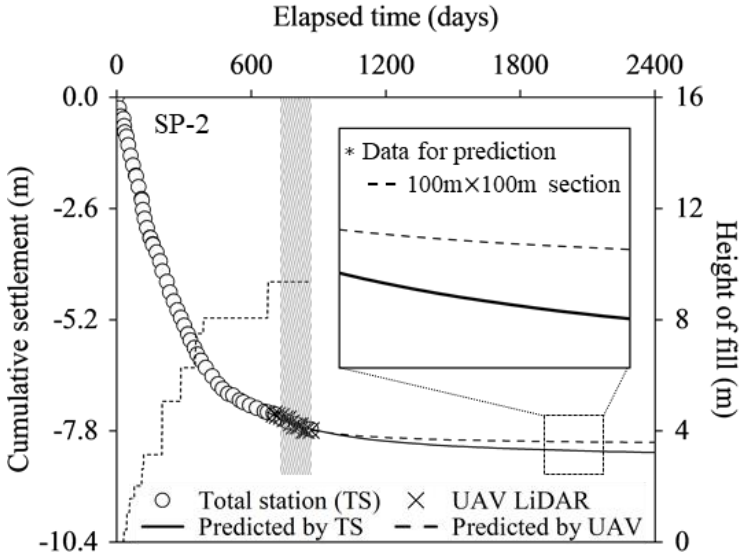

(f) Section of 100m×100m from SP-2

Figure 6.2 Settlement prediction results based on hyperbolic method according to section size

Table 6.1 Prediction accuracy of final settlement according to section size

Case	10m×10m		50m×50m		100m×100m	
	Error (m)	Error (%)	Error (m)	Error (%)	Error (m)	Error (%)
1	0.01	0.08	0.23	2.71	0.36	4.23
2	0.04	0.41	0.08	0.90	0.23	2.40

Fig. 6.3 presents the results of settlement predictions based on the number of UAV LiDAR measurements conducted after the final fill. The settlement predictions were performed using the hyperbolic method with the UAV LiDAR data collected at intervals of two weeks, specifically for four, five, six, and seven measurements. These predictions were then compared to the actual

settlement predictions based on the settlement plates. Table 6.2 depicts the prediction accuracy of final settlement according to the number of measurements. When the settlement predictions were based on seven measurements, the errors in the final settlement ranged from 0.04 to 0.08m, with an error ratio of within 0.9% relative to the final settlement, indicating a high level of accuracy. In the case of six measurements, the errors in the final settlement ranged from 0.11 to 0.15m, with error ratios of 1.1 to 1.7%. For four and five measurements, the errors in the final settlement ranged from 0.14 to 0.47m, with error ratios of 1.6 to 5.0% relative to the final settlement. It was observed that the prediction accuracy improved as the number of measurements increased. Moreover, it is determined that using seven or more measurement data ensures a high level of prediction accuracy.

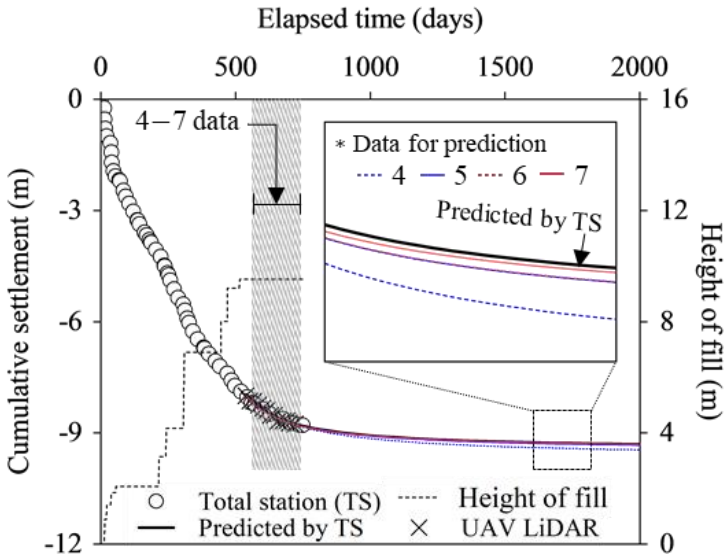

(a) Settlement plate SP-2

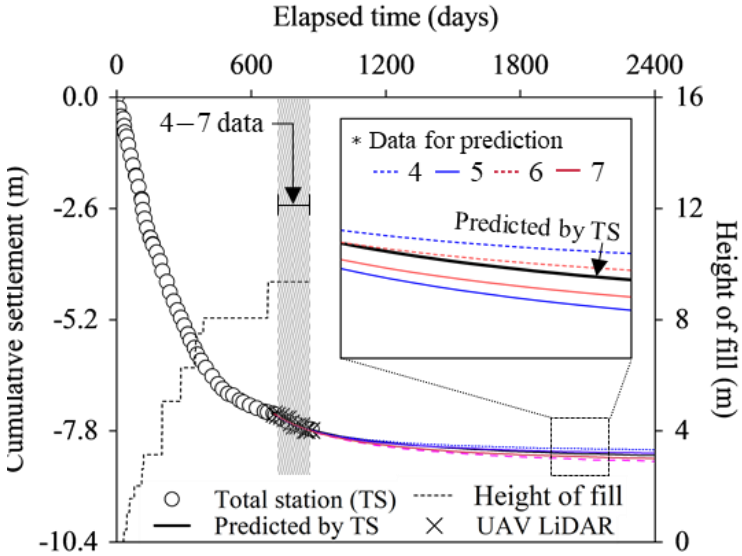

(b) Settlement plate SP-2

Figure 6.3 Settlement prediction results based on number of measurements

Table 6.2 Prediction accuracy of final settlement according to number of measurements

Case	Four		Five		Six		Seven	
	Error (m)	Error (%)	Error (m)	Error (%)	Error (m)	Error (%)	Error (m)	Error (%)
1	0.26	3.03	0.14	1.60	0.15	1.76	0.04	0.50
2	0.47	5.00	0.23	2.49	0.11	1.12	0.08	0.87

6.3 Consolidation Settlement Monitoring

The settlement of the entire site was determined based on the DEM re-projected using the average settlement of the 10m×10m section determined earlier. This process resulted in the generation of a DEM consisting of 2478 grids, dividing the entire site into distinct zones. Fig. 6.4 presents a visualization of the cumulative settlement occurring throughout the site over a period of 10 months, based on the UAV LiDAR measurements. The settlement distribution within each filling section of the entire site was visualized by delineating them with solid lines, enabling the assessment of settlement variations within each section. Due to variations in soil profiles and soil properties across the site, the settlement patterns exhibit different characteristics. Thus, settlement predictions were performed in order to determine the relative settlement ratios with respect to the final settlement. Fig. 6.5 illustrates the final settlement estimated through hyperbolic methods for all zones. For settlement predictions, data collected from a minimum of 7 measurements taken after the final fill were prioritized. In cases where measurement data was limited, analysis was performed using less than 7 measurements. Fig. 6.6 presents the visualization of the degree of consolidation based on the final settlement using the hyperbolic method throughout the entire site. The analysis of degree of consolidation revealed that it is distributed within the range of 60% to 100%. Overall, these findings suggest that the visualization of degree of consolidation during preloading can provides valuable insights for monitoring the consolidation settlement.

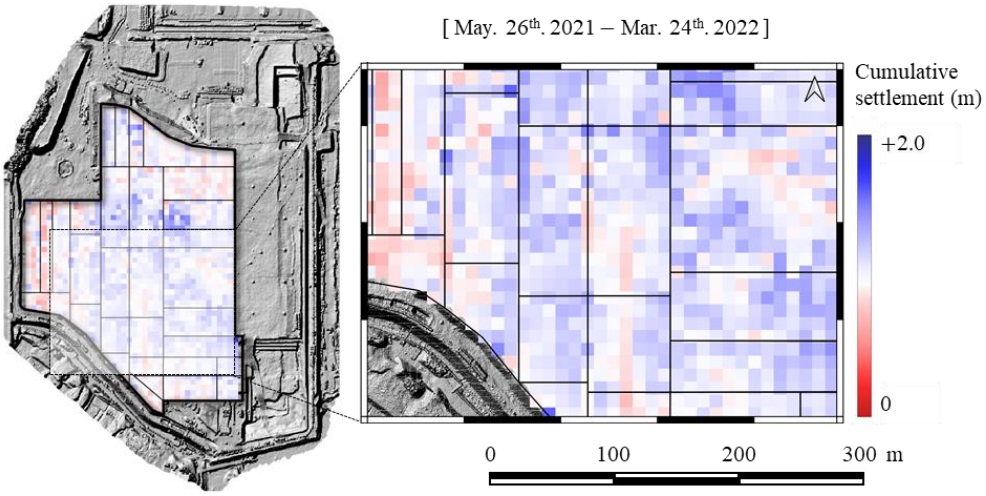

Figure 6.4 Cumulative settlement during UAV LiDAR monitoring

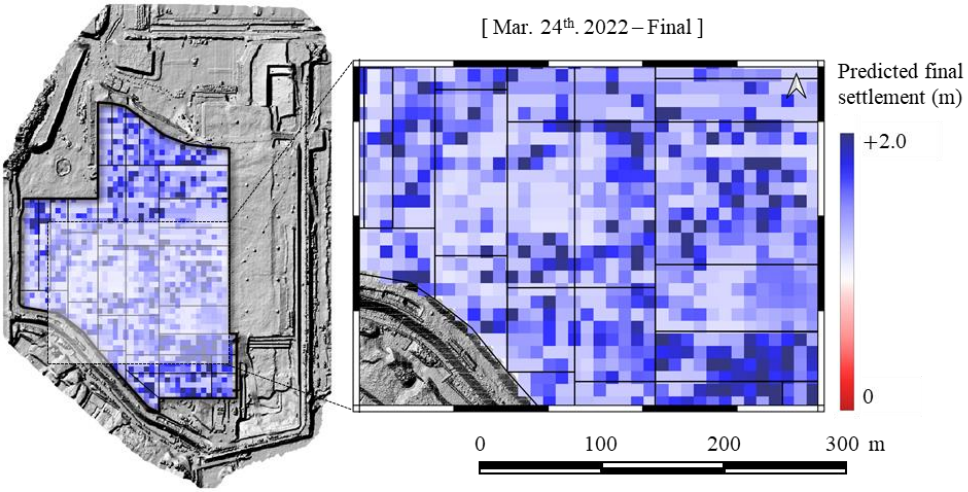

Figure 6.5 Final settlement predicted by hyperbolic method during UAV LiDAR monitoring

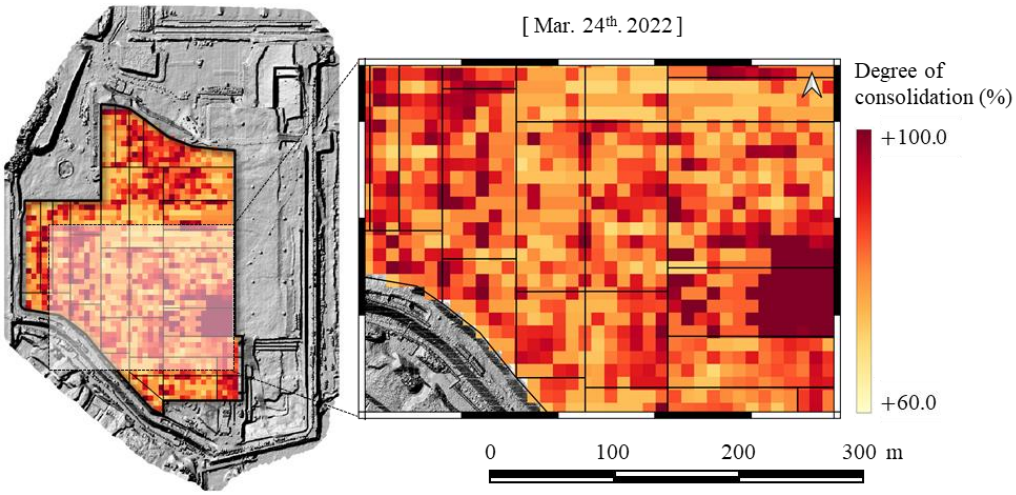

Figure 6.6 Degree of consolidation according to hyperbolic method during UAV LiDAR monitoring

6.4 Summary

In this study, settlement predictions based on the hyperbolic method were performed to determine the optimal size for managing settlement in the entire site. Settlement predictions were conducted and the accuracy of the predictions was compared by calculating the final settlement. The results revealed that performing settlement predictions for a 10m×10m section yielded a higher prediction accuracy. Additionally, an analysis was conducted on the minimum number of measurements required for settlement predictions, considering the longer measurement intervals of UAV LiDAR compared to settlement plate measurements. It was confirmed that conducting measurements at least six times at two-week intervals after the final fill ensures a high accuracy in predicting the final settlement. Furthermore, based on the analysis of section size and measurement frequency, the cumulative settlement, final settlement, and degree of consolidation for the entire site were calculated and visualized, proposing their utilization in settlement monitoring.

Chapter 7 Conclusions

In this study, UAV LiDAR was used to monitor the consolidation settlement behavior induced by preloading during construction at Busan Newport. First, the data processing of 3D point cloud was conducted. Second, the distribution of consolidation settlement was visualized. Third, settlement prediction based on hyperbolic method was performed. The result can be utilized for settlement monitoring during preloading on reclaimed land.

(1) First, the optimal denoising technique was selected by comparing three techniques for different conditions: flat ground; construction materials; and slope ground. Among the three conditions and three methods considered, the SOR method was identified as the optimal method for denoising UAV LiDAR data. Interpolation analysis was then performed on the bare-earth and settlement plate to determine the optimal grid size of DEM. The optimal grid size was determined to be 50cm×50cm by comparing the results with GPS and TS measurements. Additionally, the CSF method was employed for bare-earth filtering, with the optimal parameters selected based on the Cohen's kappa coefficient.

(2) Second, the distribution of monthly settlement rate was analyzed based on two conditions at reference section: during staged loading; after final loading. Based on the analysis of monthly settlement rate, a deviation of 0.25m/month was detected, indicating the occurrence of potential differential settlement.

Furthermore, distribution of cumulative settlement was reviewed according to section size: 10m×10m; 50m×50m; 100m×100m. The section size of 100m×100m was assumed based on the practical spacing of settlement plates. Moreover, section sizes of 10m×10m and 50m×50m were considered to propose the optimal section size for settlement monitoring. The smaller section sizes captured more localized settlement behavior, while larger section sizes exhibited significant variances. Consequently, it was concluded that the practical spacing of 100m×100m is not suitable for representing the entire construction site. Smaller spacing, such as 10m×10m, is necessary for comprehensive settlement monitoring.

(3) Third, settlement prediction using the hyperbolic method was conducted. To ensure accurate predictions, the optimal section size was determined by comparing the predicted final settlement based on different section sizes. The section size of 10m×10m, 50m×50m, 100m×100m resulted in errors of 4cm, 8cm, and 23cm, respectively. Thus, the section size of 10m×10m was identified as the optimal choice. Additionally, the required number of measurements was investigated. Four scenarios were examined, increasing the number of measurements from four to seven. The results showed that when using seven measurements, the prediction error was below 1%. Consequently, the optimal number of measurements was determined to be seven. Through the proposed analysis, the degree of consolidation across the entire site was explored. The findings of this study suggest that UAV LiDAR techniques can be utilized for monitoring the consolidation settlement at construction sites on reclaimed land.

References

Choi, Y., Park, S., & Kim, S. (2022). Development of Point Cloud Data-Denoising Technology for Earthwork Sites Using Encoder-Decoder Network. *KSCE Journal of Civil Engineering*, *26*(11), 4380–4389.

Choo, H. W., Lee, W. J., Hong, S. J., & Lee, C. H. (2016). Application of the dilatometer test for estimating undrained shear strength of Busan New Port clay. *Ocean Engineering*, *115*, 39–47.

Chung, S. G., Giao, P. H., Kim, G. J., & Leroueil, S. (2002). Geotechnical properties of Pusan clays. *Canadian Geotechnical Journal*, *39*(5), 1050–1060.

Chung, S. G., Kim, G. J., Kim, M. S., & Ryu, C. K. (2007). Undrained shear strength from field vane test on Busan clay. *Marine Georesources and Geotechnology*, *25*(3–4), 167–179.

Escolano, S., Morell, V., Rodríguez, J. G., & Cazorla, M. (2013). Point cloud data filtering and downsampling using growing neural gas. *The 2013 International Joint Conference on Neural Networks (IJCNN)*, 1–8.

Fei, X., Asce, S. M., Zekkos, D., & Asce, M. (2013). Factors Influencing Long-Term Settlement of Municipal Solid Waste in Laboratory Bioreactor Landfill Simulators. *Journal of Hazardous, Toxic, and Radioactive Waste*, 17(4), 259-271.

Feng, W. Q., Yin, J. H., Chen, W. B., Tan, D. Y., & Wu, P. C. (2020). A new simplified method for calculating consolidation settlement of multi-

layer soft soils with creep under multi-stage ramp loading. *Engineering Geology*, *264*.

Fleishman, S., Cohen-Or, D., & Silva, C. T. (2005). Robust moving least-squares fitting with sharp features. *ACM Transactions on Graphics*, *24*(3), 544–552.

Han, X. F., Jin, J. S., Wang, M. J., Jiang, W., Gao, L., & Xiao, L. (2017). A review of algorithms for filtering the 3D point cloud. *Signal Processing: Image Communication*, *57*, 103–112.

Hu, X., Oommen, T., Lu, Z., Wang, T., & Kim, J. W. (2017). Consolidation settlement of Salt Lake County tailings impoundment revealed by time-series InSAR observations from multiple radar satellites. *Remote Sensing of Environment*, *202*, 199–209.

Inzerillo, L., Di Mino, G., & Roberts, R. (2018). Image-based 3D reconstruction using traditional and UAV datasets for analysis of road pavement distress. *Automation in Construction*, *96*, 457–469.

Kim, D., Kim, K., Ko, S., Chae, Y., & Lee, W. (2013). Influence of estimation method of compression index on spatial distribution of consolidation settlement in Songdo New City. *Engineering Geology*, *152*(1), 172–179.

Kim, D., Ryu, D., Lee, C., & Lee, W. (2013). Probabilistic evaluation of primary consolidation settlement of Songdo New City by using kriged estimates of geologic profiles. *Acta Geotechnica*, *8*(3), 323–334.

Kim, J., Cho, W., & Chung, C.-K. (2016). Assessment of deformation during

consolidation using digital image analysis. *Japanese Geotechnical Society Special Publication*, *4*(3), 49–53.

Kim, J., Lee, S., Seo, J., Lee, D. E., & Choi, H. S. (2021). The Integration of Earthwork Design Review and Planning Using UAV-Based Point Cloud and BIM. *Applied Sciences*, *11*(8), 3435.

Lee, K., & Lee, W. H. (2022). Earthwork Volume Calculation, 3D Model Generation, and Comparative Evaluation Using Vertical and High-Oblique Images Acquired by Unmanned Aerial Vehicles. *Aerospace*, *9*(10), 606.

Lee, K. W., & Park, J. K. (2019). Comparison of UAV image and UAV lidar for construction of 3D geospatial information. *Sensors and Materials*, *31*(10), 3327–3334.

Lin, Y.-C., Cheng, Y.-T., Zhou, T., Ravi, R., Hasheminasab, S. M., Flatt, J. E., Troy, C., & Habib, A. (2019). Evaluation of UAV LiDAR for mapping coastal environments. *Remote Sensing*, *11*(24), 2893.

Martín-Antón, M., Negro, V., Del Campo, J. M., López-Gutiérrez, J. S., & Esteban, M. D. (2016). Review of coastal land reclamation situation in the world. *Journal of Coastal Research*, *1*(75), 667–671.

Muhammed, J. J., Jayawickrama, P. W., & Osire, S. E. (2020). Uncertainty analysis in prediction of settlements for spatial prefabricated vertical drains improved soft soil sites. *Geosciences*, *10*(2), 42.

Ramirez, R. A., & Kwon, T. (2022). Sentinel-1 Persistent Scatterer Interferometric Synthetic Aperture Radar (PS-InSAR) for Long-Term

Remote Monitoring of Ground Subsidence: A Case Study of a Port in Busan, South Korea. *KSCE Journal of Civil Engineering*, *26*(10), 4317–4329.

Rauhala, A., Tuomela, A., Davids, C., & Rossi, P. M. (2017). UAV Remote Sensing Surveillance of a Mine Tailings Impoundment in Sub-Arctic Conditions. *Remote Sensing*, *9*(12), 1318.

Sakleshpur, V. A., & Prezzi, M. (2018). Ground engineering using prefabricated vertical drains: A review. *Geotechnical Engineering Journal of the SEAGS & AGSSEA*, *49*(1).

Shi, G., Lin, H., Bürgmann, R., Ma, P., Wang, J., & Liu, Y. (2019). Early soil consolidation from magnetic extensometers and full resolution SAR interferometry over highly decorrelated reclaimed lands. *Remote Sensing of Environment*, *231*.

Siebert, S., & Teizer, J. (2014). Mobile 3D mapping for surveying earthwork projects using an Unmanned Aerial Vehicle (UAV) system. *Automation in Construction*, *41*, 1–14.

Suneel, M., Park, L. K., & Im, J. C. (2008). Compressibility characteristics of Korean marine clay. *Marine Georesources and Geotechnology*, *26*(2), 111–127.

U.S. Army Corps of Engineers. (2021). Engineering and Design – REMOTE SENSING (EM 1110-1-2910). *U.S. Army Corps of Engineers*, Washington, D.C.

Yang, Y. H., Xu, Q., Hu, J. C., Wang, Y. S., Dong, X. J., Chen, Q., Zhang, Y.

J., & Li, H. L. (2022). Source Model and Triggered Aseismic Faulting of the 2021 Mw 7.3 Maduo Earthquake Revealed by the UAV-Lidar/Photogrammetry, InSAR, and Field Investigation. *Remote Sensing*, *14*(22), 5859.

Yu, Q., Yan, X., Wang, Q., Yang, T., Lu, W., Yao, M., Dong, J., Zhan, J., Huang, X., Niu, C., & Zhou, K. (2021). A Spatial-Scale Evaluation of Soil Consolidation Concerning Land Subsidence and Integrated Mechanism Analysis at Macro-, and Micro-Scale: A Case Study in Chongming East Shoal Reclamation Area, Shanghai, China. *Remote Sensing 2021, Vol. 13, Page 2418*, *13*(12), 2418.

Zhang, B., Wang, R., Deng, Y., Ma, P., Lin, H., & Wang, J. (2019). Mapping the Yellow River Delta land subsidence with multitemporal SAR interferometry by exploiting both persistent and distributed scatterers. *ISPRS Journal of Photogrammetry and Remote Sensing*, *148*, 157–173.

Zhang, W., Qi, J., Wan, P., Wang, H., Xie, D., Wang, X., & Yan, G. (2016). An Easy-to-Use Airborne LiDAR Data Filtering Method Based on Cloth Simulation. *Remote Sensing*, *8*(6), 501.

초 록

대심도 연약지반의 압밀침하 관리 시 넓은 부지에 비해 상대적으로 소수의 계측기가 설치된다. 지반 조건의 불확실성에 의해 침하를 측정하지 않은 위치에서는 과도한 침하가 발생될 수 있다. 최근에는 원격 탐사 기술을 기반으로 지반 변형을 분석하는 연구가 다수 수행되고 있다. 그러므로, 본 연구에서는 드론라이다 계측을 활용하여 부산신항 건설현장 전체 부지에 대한 압밀침하 모니터링 방법을 제안하였다.

먼저 3차원 포인트 클라우드의 데이터 처리가 수행되었다. 평지, 건설자재, 경사지를 대상으로 노이즈 제거 기법들을 비교한 결과, SOR 기법이 UAV LiDAR 데이터의 노이즈 제거를 위한 최적 기법으로 확인되었다. 최적의 격자 크기는 GPS와 TS 측정 결과와 비교하여 50cm×50cm로 결정되었다.

다음으로, 침하 거동의 분포에 대한 분석이 수행되었다. 레퍼런스 구역에 대한 월간 침하속도 분석 결과, 0.25m/month의 편차가 관측되어, 잠재적인 부등침하가 발생할 수 있음을 시사하였다. 다양한 구역 크기에 따른 누적 침하량 분석 결과, 작은 구역은 국부적인 침하 거동을 파악할 수 있지만 큰 구역은 침하 분포에 있어서 상당한 변동성을 나타내었다. 따라서, 현행 지표침하판 배치 간격인 100m×100m의 경우, 건설 현장의 전체 침하를 대표하기에는 적합하지 않다는 결론이 도출되었다.

마지막으로, 쌍곡선법 기반 침하예측이 수행되었다. 정확한

예측을 위해, 다양한 구역 크기에 따른 예측 최종 침하량을 비교함으로써 최적의 구역 크기가 결정되었다. 분석 결과, 10m×10m의 구역 크기가 최적으로 선정되었으며, 4cm의 오차가 발생하였다. 또한, 계측 횟수에 따른 침하예측 정확도가 평가되었다. 7개의 계측을 이용한 예측 결과 1% 이내의 예측 오차를 보였으며, 이를 최적의 계측 횟수로 결정하였다. 제안된 분석 방법을 통해 전체 현장에 대한 쌍곡선법 기반 압밀도가 산정되었다. 본 연구 결과는 준설매립 시공 현장에서 선행재하공법 중 발생하는 압밀침하 모니터링에 활용될 수 있다.

주요어 : 드론, 라이다 데이터 처리, 압밀 침하, 매립, 침하 예측

학번 : 2021-28403